TÜBİTAK

Turkish Journal of Chemistry

http://journals.tubitak.gov.tr/chem/

Research Article

Turk J Chem
(2018) 42: 1479 – 1498
© TÜBİTAK
doi:10.3906/kim-1803-18

Fabrication and electrochemical performance of $La_{0.595}V_{0.005}Sr_{0.4}MnO_{3-\delta}$ (LV05SM) cathode material for solid oxide fuel cells

Ayşenur Eslem KISA, Oktay DEMİRCAN*
Department of Chemistry, Faculty of Arts and Sciences, Boğaziçi University, İstanbul, Turkey

Received: 06.03.2018 • **Accepted/Published Online:** 14.06.2018 • **Final Version:** 06.12.2018

Abstract: This study reports the effect of vanadium on the crystal structure and electrical and electrochemical properties of $La_{0.6-x}V_xSr_{0.4}MnO_{3-\delta}$ (x = 0.005–0.1) perovskite-based cathode materials in solid oxide fuel cells. Crystal structure, morphology, and porosity of prepared cathode materials are characterized by X-ray diffraction, X-ray photoelectron spectroscopy (XPS), and scanning electron microscopy. Using XPS analysis it was established that the La^{3+} cation is exchanged by the $V^{4+/5+}$ cation in the perovskite structure. This ion replacement improves the ionic conductivity and catalytic activity for oxygen reduction reaction in the perovskite structure, presumably due to the smaller size of the $V^{4+/5+}$ cation than the La^{3+} ion. Oxygen partial pressure-related polarization experiments suggest that the adsorption-desorption process and the reactions controlled by the atomic oxygen diffusion process followed by charge transfer are the cathode reaction rate-limiting steps.

Key words: Solid oxide fuel cells, perovskite, oxygen reduction reaction, symmetric cells, electrochemical impedance spectroscopy

1. Introduction

Recent interest in building a hydrogen-based economy and reducing environmental pollution has propelled the research on fuel cell innovation, especially in the area of solid oxide fuel cells (SOFCs).[1] SOFCs, being electrochemical energy conversion devices, have noteworthy benefits over the ordinary power generation technologies. They are electrochemical devices that convert chemical energy into electrical energy with high efficiency, because their effectiveness is independent of the Carnot cycle of a heat engine.[2] Additional efficiency can be achieved when the generated energy is utilized with combined heat and power or gas turbine systems.[3]

Among the several types of fuel cells, SOFCs possess several attractive features, such as high energy conversion efficiency, fuel flexibility, solid-state parts, high power density, low greenhouse gas emissions, lower system noise, and environmental friendliness.[4] Similar to other fuel cells, SOFC systems consist of the electrodes (anode and cathode) and an electrolyte. The anode side of the cell is fed with the fuel, e.g., hydrogen, and an oxidant such as air is flowed over the cathode side, while the electrolyte transfers the oxide ions or protons from cathode to anode or vice versa.

The very first SOFC was developed by Baur and Preis in 1937, which operated at 1000 °C.[5] Although several decades have passed since their introduction, commonly used SOFCs still work at high temperatures (close to 900 °C).[6] This leads to material degradation and results in high production costs, thus hindering their

*Correspondence: oktay.demircan@boun.edu.tr

economic feasibility. Hence, lowering their operation temperature to an intermediate range (600–800 °C) can reduce the cost and expand their lifetime.[7]

Furthermore, high working temperatures limit the choice of materials used in SOFCs, since degradation during operation will limit the lifetime of SOFCs.[8] An obvious site of degradation is the air electrode, where the oxygen reduction reaction (ORR) occurs, which is generally the main rate-limiting step for the performance of the whole SOFC system.[9] Hence, one of the most important goals in the area of SOFCs is the development of new cathode materials that offer desired electrochemical performance in thet intermediate temperature range (600–800 °C).[10] Required attributes for such cathode materials are high electronic and ionic conductivity, thermal expansion coefficient values similar to other SOFC compartments, large triple phase boundary (TPB) area, high performance of the catalyst for the dissociation of oxygen, and low cathode resistance.[11] Most of these requirements are met by mixed ionic and electronic conductors (MIECs) and their composites. These materials provide synchronized transport of both electrons and ions, hence enhancing the potential reaction sites that are at the TPBs where the active side of the electrode, the electrolyte, and the gases meet. MIECs generally derive their distinctive properties from their special crystal structure, often referred to as the perovskite structure. The ideal oxide perovskite structure ABO_3 consists of a cubic array of corner sharing BO_6 octahedral with the A cation at the body center position. However, nonideal A and B ionic radii create distortions in the cubic lattice (often orthorhombic or rhombohedral),[12] and these intrinsic alterations lead to vacancies at lattice crystals that exhibit ionic conductivity.[13]

Perovskite materials such as $La_{1-x}Sr_xMnO_{3-\delta}$ (LSM) with x between 0.15 and 0.50 are the most commonly used and studied cathode materials for standard SOFCs.[14] These Sr-doped lanthanum perovskites stay stable both in oxygen excess-oxidizing and oxygen deficient-reducing gas atmospheres.[15] Oxygen deficiency leads to oxygen vacancies while oxygen excess results in metal site vacancies, which improves electrode properties due to facilitation of activation of O_2 in the ORR. However, the ionic conductivity of LSM is extremely low due to the low concentration of oxide ion vacancies.[16] This causes practical limitations and restrictions for the application of LSM, especially at low temperatures (<800 °C). As the working temperature of SOFC system decreases below 800 °C, the oxide ion conductivity for the traditional cathode materials like LSM distresses the ORR performance.[17] Therefore, incorporation of a material or doping with another metal with comparable higher oxide ion conductivity may improve the cathode performance.

Vanadium is one of the most abundant and widely allocated metals in the earth's crust and is found in nearly 150 different minerals.[18,19] The most widespread use of vanadium is in catalysis, and vanadium oxide-based catalysts are used in the production of important chemicals such as sulfuric acid and phthalic anhydride, and in the reduction of environmental pollution like NO_x from vent-gas of power plants.[20–27] Multiple oxidation states for V such as +2, +3, +4, and +5 provide it with extra stability under oxidizing and reducing conditions.[28] Also, due to their multivalent oxide structures, vanadium oxides are commonly used for selective catalytic reduction reactions.[29]

In this study, the perovskite oxide material, $La_{0.6-x}V_xSr_{0.4}MnO_{3-\delta}$ (x = 0.005–0.1) is systematically synthesized and characterized by X-ray diffraction (XRD), X-ray photoelectron spectroscopy (XPS), and scanning electron microscopy (SEM). The LV05SM (x = 0.005) composition is preferred according to these analyses and investigated for direct application as intermediate-temperature SOFC cathode material. In particular, the area-specific resistance (ASR) properties, polarization resistances (R_p), and electrochemical performance under oxidizing atmosphere using two types of electrolytes, yttria-stabilized zirconia (YSZ) and gadolinium-

doped ceria (GDC), are studied to evaluate the performance of LV05SM in a symmetrical cell configuration by electrochemical impedance spectroscopy (EIS).

2. Results and discussion

The $La_{0.6-x}V_xSr_{0.4}MnO_{3-\delta}$ (LVxSM, x = 0.005–0.1) powders were synthesized using a sol-gel technique, as described in Section 3.

2.1. XRD analysis of $La_{0.6-x}V_xSr_{0.4}MnO_{3-\delta}$ (LVxSM)

Phase homogeneity of various $La_{0.6-x}V_xSr_{0.4}MnO_{3-\delta}$ (x = 0.005–0.1) powders was compared using the XRD plots (Figure 1). It was observed that $La_{0.6-x}V_xSr_{0.4}MnO_{3-\delta}$ materials crystallize in a rhombohedral structure, similar to the $La_{1-x}Sr_xMnO_3$ systems.[30] The rhombohedral distortion of the perovskite octahedra is characterized by the splitting of the principal reflection, which appears as a double peak in the range 2θ = 32–33°.[31] Figure 1 presents typical XRD patterns of $La_{0.6-x}V_xSr_{0.4}MnO_{3-\delta}$ (x = 0.005–0.1) obtained at 1100 °C. The patterns suggest that the LVxSM samples have a single-phase perovskite structure without any detectable impurity phases up to x = 0.01 and the $Sr_6V_6O_{19}$ secondary phase at 2θ values of 29.6°started to form when V content was above x = 0.01. This indicates that LVxSM can form a solid solution with V content of x $\leq$ 0.01. No resistive phases, either $La_2Zr_2O_7$ or $SrZrO_3$, are detected in XRD for the LV10SM cathode material. A well-defined perovskite oxide phase can be seen from Figure 1. However, there are some extra peaks with small size in the XRD pattern. It was deduced that they belong to strontium vanadium oxide $Sr_3(VO_4)_2$ by XRD phase analysis software. $Sr_3(VO_4)_2$ is a kind of perovskite material-related MIEC and is not considered to be detrimental to the SOFC cathode. However, it is obvious that there is a distortion from the perovskite crystallinity. This suggests that the limit of V doping in this series of $La_{0.6-x}V_xSr_{0.4}MnO_{3-\delta}$ materials should not exceed 10 mol%. As can clearly be seen from Figure 1, the diffraction pattern confirms the pure rhombohedral phases of LV05SM ($La_{0.6-x}V_xSr_{0.4}MnO_{3-\delta}$ where x = 0.005) and substitution of V at a level of 0.5 mol% did not change the crystallinity of the sample. Since LV05SM has no impurity, these results suggest that LV05SM is a potential candidate for application as a cathode material and hence it was decided to analyze only LV05SM for its physical and electrochemical properties from here on.

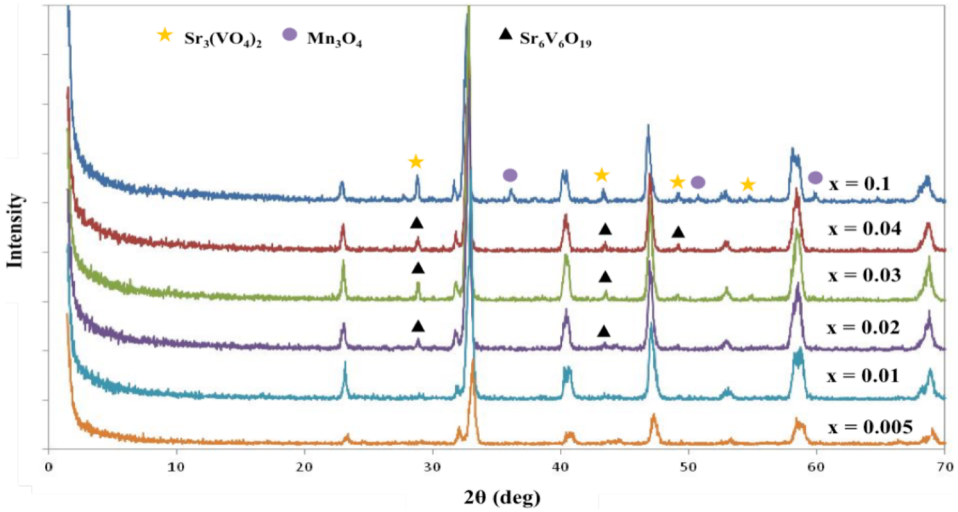

Figure 1. XRD patterns of $La_{0.6-x}V_xSr_{0.4}MnO_{3-\delta}$ (x = 0.005–0.1) samples.

2.2. XPS analysis of LV05SM

The chemical environments of La, V, Sr, and Mn ions were estimated by curve-fitting of La3d, V2p, Sr3d, and V2p spectra, as shown in Figure 2. No peaks of elements other than La, Mn, Sr, and V except C1s are observed on the survey spectrum (Figure 2).

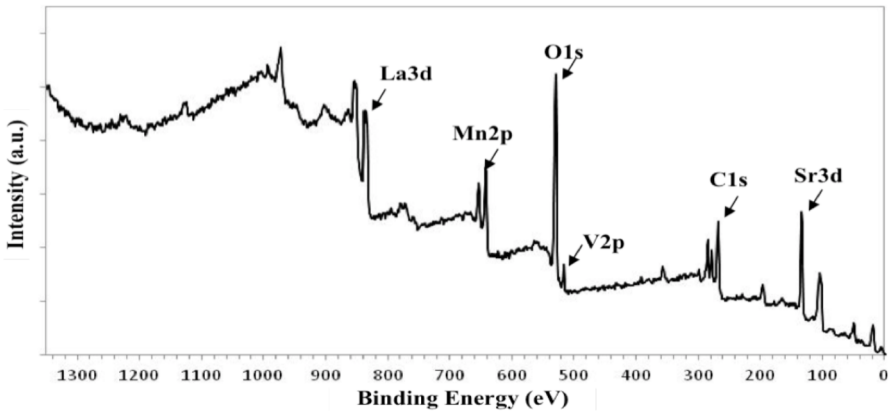

Figure 2. XPS spectra survey analysis at room temperature for LV05SM samples.

The La3d states of LV05SM are shown in Figure 2 (details are given in Supplementary materials). The La3d3/2 peak of the sample is divided into two peaks at binding energies of 853.38 and 850.68 eV, and the corresponding binding energy of La3d5/2 is 837.3 and 833.5 eV. The energy difference between the 3d3/2 and 3d5/2 levels is approximately equal to 17 eV. The binding energies and the multiplet splitting agree well with reported values for La^{3+} compounds.[32]

The binding energies of the V2p levels are 515.88 and 516.6 eV for V2p3/2 and V2p1/2, respectively, in Figure 2 (details are given in Supplementary materials). These can be assigned to vanadium in a V^{4+} and V^{5+} state.[33] The Sr 3d core-level spectra of the samples contain a doublet as shown in Figure 2 (details are given in Supplementary materials), whose binding energies are 132.2 and 133.08 eV, which can be assigned as Sr3d5/2 and Sr3d3/2, respectively, indicating that Sr ions are located in two different environments. Regarding the binding energy of the Sr3d5/2 peak, the component at 132.2–132.7 eV comes from Sr ions incorporated into the perovskite structure and the one observed for Sr3d3/2 can be assigned to $SrCO_3$.[34] From the XPS spectra, we can conclude that the binding energies are very close to those observed for similar compounds,[35] which can be attributed to the Sr^{2+} ions in LV05SM.

Also, the Mn2p XPS spectra of LV05SM can be seen in Figure 2 (details are given in Supplementary materials). These spectra display a broad emission line with a maximum near at 641.2 eV for Mn2p3/2 and 653.08 eV for Mn2p1/2 emissions. According to the binding energy of Mn2p3/2, the oxidation state of Mn ions is between $+3$ and $+4$.[36]

2.3. SEM analysis of LV05SM cathode surface

Surface morphology and the cross-section of the symmetric cell cathode were investigated in detail using SEM (Figure 3). The surface view in Figure 3a indicates the porosity of the LV05SM cathode material with YSZ electrolyte. The cross-sectional view in Figure 3b shows the thickness of the cathode and the morphology difference between cathode and electrolyte.

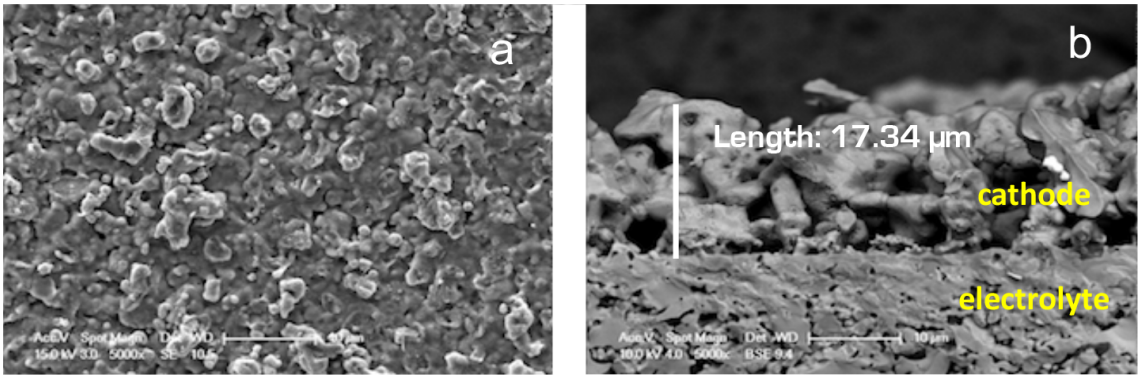

Figure 3. SEM images of LV05SM: a) surface and b) cross-section views of the cathode-electrolyte interface.

A uniform distribution of particles and pores is observed on the cathode, both at the interface of the cathode/electrolyte and on top of the cathode. No special variation in microstructures is observed across individual layers. Since the sintering temperature is 1300 °C, the adhesion between the cathode and electrolyte is strong. This provides better oxide ion conductivity from the cathode to the electrolyte material; hence, better performance of the cell is expected. The average pore size of the cathode material is 4–5 µm and the approximate grain size is 3–4 µm. The thickness of the cathode is measured as approximately 17 µm, as seen in Figure 3b. Since the cathode paste was applied to the surface of the electrolyte, this thickness is reasonable as an active cathode layer. Furthermore, the thickness of the cathode can be optimized by employing different types of application methods, such as screen-print and tape casting.

2.4. Electrical conductivity – four-probe measurement results

The electrical conductivity was measured by the four-probe DC method on sintered rectangular bars. The measurements were performed upon heating from 400 to 800 °C in air, and with a heating rate of 1 °C/min. Four gold (Au) wire contacts were made, which were painted with gold conducting paint (Heraeus). Two current contacts were attached at the bar edges, with two voltage contacts in between at a distance l. The sample was then fired at 500 °C for 1 h to allow complete adhesion of the electrodes and reduction of the contact resistance. The sample was then placed in a horizontal tube furnace. In this method, an electric current is passed through a bar of the sample and a voltage drop is measured across a distance in the middle of the sample. The sample was left at each temperature at which measurements were taken. The electrical conductivity σ was calculated by the following equation: $R = \rho\frac{l}{A}$, where R is the electrical resistance, A is the cross-sectional area of the rod, l is the thickness of the cathode, and ρ is the specific resistance. Electrical conductivity values (σ) were obtained through the inverse of the specific resistance.

The conductivity of LV05SM material under air was measured using a four-probe DC method. The electrical conductivity of the LV05SM sample as a function of temperature and the logarithm of electrical conductivity vs. reciprocal temperature in air are shown in Figure 4. LSM is known as a p-type semiconductor with electronic holes as charge carriers and essentially this hole motion in the d-orbital energy levels of manganese is the reason for the electrical conductivity.[37] This is explained by the small polaron hopping of electron holes between Mn^{4+} and Mn^{3+} sites on octahedral corners. The conduction mechanism was completed by the hopping of electrons between multivalent metal ions at the B-site and oxygen ion following the way along B–O–B bonds. The equilibrium between Mn^{4+} and Mn^{3+} ions is controlled by a thermally activated disproportionation of Mn^{3+} in crystalline solids:[38]

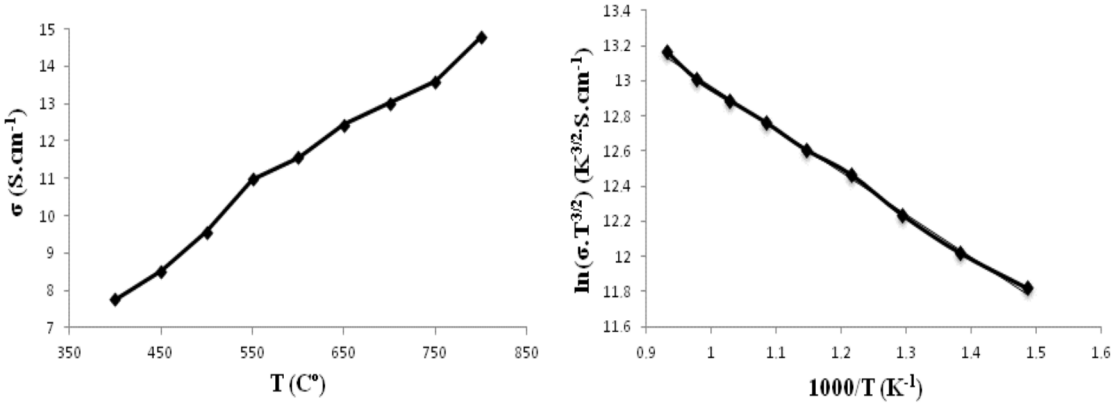

Figure 4. Temperature dependence of the electrical conductivity of LV05SM sample sintered at 1100 °C.

$$2Mn_{oct}^{3+} \leftrightarrow Mn_{oct}^{4+} + Mn_{oct}^{2+}.$$

The Mn^{2+} ion is formed due to disproportionation but the conduction process occurs just via the hopping of carriers between Mn^{4+} and Mn^{3+} sites. As a result of charge transfer from the Mn^{3+} site to the neighboring Mn^{4+} site, the conduction process is assumed to develop, such as jumps of p-type carriers over available sites.[39] Since the electronic conductivity is usually 100–1000 times higher than the ionic conductivity for these kinds of oxides, the measured values reported herein are attributed to the electronic conductivity alone.[40] Generally, the conductivity gradually increases with increasing temperature. However, there is a fluctuation in conductivity at about 550 °C, which may be due to the loss of the lattice oxygen, leading to more oxygen vacancies as a result of the thermally induced lattice oxygen losses,[41] as expressed by the equation below:[42]

$$O_o^x + 2B_B^{\bullet} \rightarrow V_O^{\bullet\bullet} 2B_B^x + \frac{1}{2}O_2(g),$$

where $B_B^{\bullet}$ refers to B^{4+} localized on the B^{3+} site and B_B^x stands for B^{3+}. O_o^x is the lattice oxygen and $V_O^{\bullet\bullet}$ represents the oxygen vacancy. However, the lattice oxygen loss in p-type semiconductors at high temperatures would be the reason for the decrease of electrical conductivity, due to the reduction of charge carrier concentration (electron holes),[43] as expressed by the equation above. There is only electrical conductivity fluctuation at about 550 °C and no permanent decrease of conductivity is observed in the temperature range of 400–800 °C. This means that there is little lattice oxygen loss and thus relatively good structural stability of LV05SM. The temperature dependence of electrical conductivity is shown in Figure 4. When considering the electrical conductivity by the help of Arrhenius plot $ln(\sigma T)$ vs. $1/T$, linear behavior reveals that the electronic conductivity is because of the small polaron-hopping mechanism, which follows the way along the transition metal-oxygen-transition metal chains (B–O–B) in the perovskite structure.[10] Activation energy can be calculated by fitting the equation $\sigma = \left(\frac{C}{T^s}\right)\exp\left(\frac{E_a}{kT}\right)$, where σ is the electrical conductivity, C is the preexponential factor, T is the temperature, $k$is the Boltzmann constant, and E_a is the activation energy expressing the enthalpy of the polaron-hopping mechanism. The exponent s equals either 1 or 3/2 for adiabatic or nonadiabatic processes, respectively.

The E_a value for σT was calculated as 0.20 eV for the LV05SM sample. This value is slightly higher than that reported by Wandekar et al. as 0.14 eV for $La_{0.76}Sr_{0.19}MnO_{3-\delta}$ samples and also the results of Aruna et al., where the activation energy was reported as 0.155 eV for $La_{0.90}Sr_{0.10}MnO_{3-\delta}$.[44,45]

As seen in Figure 4 (details are given in Supplementary materials), when the conductivity of LV05SM is compared with our synthesized $La_{0.8}Sr_{0.2}MnO_3$ sample, it is noted that the activation energy is calculated as 0.15 eV. This activation energy value is nearly the same as measurements of a bulk sample of 0.12 eV by Kuharuangrong.[46] $La_{0.6}Sr_{0.4}MnO_{3-\delta}$ with higher Sr content material is synthesized in order to examine the conductivity dependence on the doping levels of Sr for $La_{1-x}Sr_xMnO_{3-\delta}$.

The electrical conductivity of the sample is measured and calculated as 86 S/cm at 800 °C with E_a of 0.099 eV. The value for electrical conductivity is less than that reported by other researchers as 320 S/cm for electrical conductivity,[47] but the same for activation energy of 0.099 eV.[48] The reason for different conductivity values is possibly differences in preparation conditions such as synthesis and calcination. The electrical conductivity at 800 °C and the maximum conductivity values, as well as the activation energies of all compositions, are calculated and summarized in Table 1.

Table 1. Calculated σ_{max}, $\sigma_{800°C}$, and E_a of specimens sintered at 1100 °C.

Composition	σ_{max}(S/cm)	$\sigma_{800\,°C}$ (S/cm)	Temp. range (°C)	E_a (eV)
$La_{0.595}V_{0.005}Sr_{0.4}MnO_3$	14.80	14.80	400–800	0.20
$La_{0.6}Sr_{0.4}MnO_3$	96.42	86.02	400–800	0.09
$La_{0.8}Sr_{0.2}MnO_3$	46.90	46.90	400–800	0.15

$LaMnO_3$ is the conventional material of choice in commercial SOFCs based on zirconia electrolytes. Electrical conductivity is enhanced by substitution of the La^{3+} site with divalent ions such as strontium or calcium. Among the alkaline earth dopants, Sr substitution is preferred for SOFC applications because the resultant perovskite forms stable compounds with high conductivity in the oxidizing atmosphere encountered at the cathode.[49] Divalent acceptor substitution (e.g., Sr^{2+}) for the trivalent A-site cation (e.g., La^{3+}) requires a balance in the electroneutrality. The introduced negative charge is compensated by an increase in valence of the B-site cations (electrical compensation).[50] Transition metals (TM) as B-site cations perform TM^{4+}/TM^{3+} couples, which act as hopping sites for electrons/holes, i.e. for n-type or p-type conductivity. When a La^{3+} ion at the A-site is replaced by a Sr^{2+} ion, an electric hole is formed on the B-site to maintain the electroneutrality, leading to increased electrical conductivity:[51]

$$LaMnO_3 \xrightarrow{xSrO} La_{1x}^{3+}Sr_x^{2+}Mn_{1x}^{3+}Mn_x^{4+}O_3.$$

The disproportionation of Mn^{3+} ions into Mn^{2+} and Mn^{4+} pairs (equation above) seems to provide a compensation mechanism, which is able to account for this apparent buffering of added Sr ions in $LaMnO_3$. $La_{1-x}Sr_xMnO_{3-\delta}$ has electrical properties on the border between that of a p-type semiconductor and a metal.[52] In this temperature range conductivity is increased with increasing temperature for LV05SM, typical of semiconductor behavior.

2.5. Electrochemical impedance spectroscopy results

The results from four-probe method measurements show that the conductivity values are lower than expected. However, there are important features other than the electrical conductivity, e.g., ionic conductivity, which is one of the main features of the cathode performance for SOFC. The most complex and least understood process in the overall SOFC-cathode mechanism is the ORR. This process is often referred to as the surface exchange

of oxygen, perhaps because it is still not known which of the many elementary reactions are rate-limiting in the overall reaction and in which order they occur. The surface exchange reaction is generally believed to consist of the following subreactions (not elementary): O_2 adsorption, O_2 dissociation, and incorporation of oxygen species into the oxide lattice and the reduction of either diatomic or monoatomic oxygen species:

$$O_{2\,(g)} + ne^- \rightarrow O^n_{2,ads},$$

$$O^n_{2,ads} + me^- \rightarrow 2O^{(n+m)}_{ads},$$

$$O^{(n+m)}_{ads} + (2nm)\,e^- + V^{\cdot\cdot}_O \rightarrow O^X_O.$$

The reduction reaction is generally considered to proceed simultaneously with the other reactions to form arbitrarily charged surface species, e.g., $O^n_{2,ads}$, O^n_{ads}, or O^n_O, depending on which reaction is the rate-limiting step.[53]

In this portion of study, to understand the ORR mechanism, complex impedance measurements were carried out on a selected number of compositions versus the oxygen partial pressure PO_2 at different temperatures. EIS data (details given in Supplementary materials) show impedance responses for the single-phase LV05SM electrode on the YSZ electrolyte measured under different oxygen partial pressures and collected at intervals of 50 °C in the temperature range from 400 to 800 °C.

It is clearly seen from the EIS data in Figure 5 that the high-frequency part of the two clearly resolved impedance contributions has an apparent shape in the Nyquist plots below the 500 °C. With increasing operating temperature, the high-frequency arc size decreased noticeably, and the arc totally disappeared at 500 °C and higher. An additional arc in the low-frequency region appeared when the operating temperature was elevated to 700 °C. The impedances of a symmetric cell may arise from both the electrodes and the electrolyte. The electrolyte typically performs as an ideal resistor and displays only a dot in the Nyquist plots at high temperatures in the investigated frequency range of 10^6 to 10^{-1} Hz. However, a semicircle associated with the oxide ion diffusion around the grain boundary of the electrolyte also appeared in the high-frequency range with the decrease in operation temperature. Similar findings have been reported before, e.g., Zhan et al. observed that the arc associated with the grain boundary ionic diffusion appeared at an operation temperature of 460 °C in the complex impedance plane plots.[54]

In order to obtain more information to properly interpret the processes involved in the cathode/electrolyte interface, a study of the influence of oxygen partial pressure in the electrode impedance as a function of temperature was carried out. The oxygen partial pressure of the atmosphere was varied between 0.01 and 0.25 atm by mixing O_2 with N_2 using mass flow controllers.

Figure 5 shows typical EIS diagrams of the LV05SM cathode measured at 400–800 °C in air for 3% – 10% – 15% – 25% O_2. They are composed of a large arc located in between the high-frequency and low-frequency zones. All Nyquist plots were fitted to the equivalent circuit of $L - R_b - (R_1{-}QPE_1) - (R_2{-}QPE_2)\cdots(R_i{-}QPE_i)$ shown in Figure 5's inset by means of Gamry software. The data fitting covers three processes in the electrode reaction; the results show good agreement between the experimental and fitted data. L is inductance caused by the device and the connect leads and R_b is the ohmic resistance of the YSZ electrolyte. The remaining components are associated with the electrode where three series-connected elements (RQ) describe the three processes that contribute to the impedance of the electrode/electrolyte interface. The numbers of R_i – QPE_i impedances (made by a resistor R_i in parallel with a constant phase element QPE_i) in series are dependent

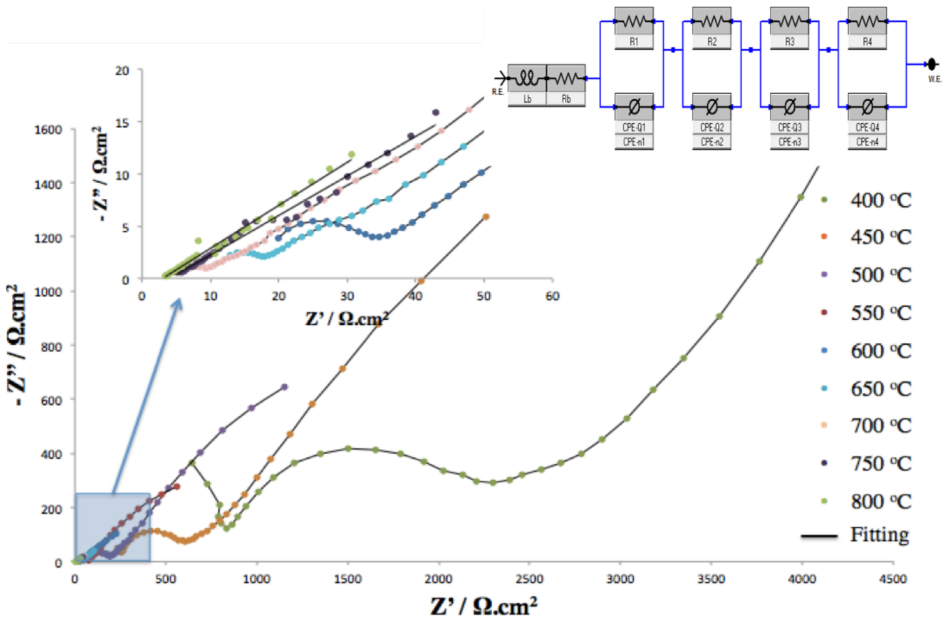

Figure 5. Impedance spectra of LV05SM cathode measured in 25% O_2 and 75% N_2 at various temperatures with data fitting. Inset: The equivalent circuits used for fitting the impedance data for 500–800 °C.

on operation temperature. The exact equivalent circuits adopted for fitting the EIS data at temperatures of 500–600 °C are fitted well to an equivalent circuit of $L-R_b-(R_1-QPE_1)-(R_2-QPE_2)-(R_3-QPE_3)$ and the temperatures of 400, 700, and 800 °C are in agreement with an equivalent circuit of $L-R_b-(R_1-QPE_1)-(R_2-QPE_2)-(R_3-QPE_3)-(R_4-QPE_4)$. The first component $(R_1\,QPE_1)$ appears as a semicircle in the high-frequency region, the second one $(R_2\,QPE_2)$ as a semicircle in the medium-frequency region, and the third one $(R_3\,QPE_3)$ as a semicircle in the low-frequency region.

With higher operation temperature, the size of the semicircle at high frequency decreased and it totally disappeared above 500 °C. This implies that the well-separated semicircle in the EIS high-frequency range of 400–500 °C may be associated with the oxide-ion transfer through YSZ electrolyte grain boundaries. The second semicircles in the EIS data are contributed by oxygen reduction over the LV05SM electrode. Impedance at high and intermediate frequencies is related to ion and electron transfer at the electrode, electrolyte, and collector/electrode interfaces, while the impedance at low frequencies is associated with noncharge transfer, such as oxygen surface exchange and gas-phase diffusion inside and outside the electrode layer.[55]

Table 2 summarizes the fitting parameters as a function of temperature for LV05SM/YSZ/LV05SM under different partial pressures of oxygen, as well as the ASR values.

The inductance value was shown but not considered, because it is not characteristic of the studied compound. It can be seen that the electrolyte resistance (R_b) as well as the four resistances (R_1, R_2, R_3, R_4) associated with the kinetics of electrode processes decrease with increasing temperature, as expected. It can also be seen that the electrolyte resistance, R_b, does not depend on the oxygen partial pressure, remaining stable at each temperature, which is in agreement with the behavior of a pure ionic conductor such as the YSZ electrolyte.

The polarization resistance (R_p) is the purely ohmic part of the electrode resistance. It can be determined as the sum of the resistances of each individual process $(R_p = R_1+R_2+R_3+R_4)$. For the symmetrical cell, the

Table 2. The fitting parameters as a function of temperature for LV05SM/YSZ/LV05SM in PO_2.

PO_2	T (°C)	400	500	600	700	800
O3	*Lb* (H)	5.09×10^{-8}	7.39×10^{-9}	5.31×10^{-6}	1.37×10^{-10}	8.44×10^{-11}
	Rb ($\Omega.cm^2$)	1.0722	0.5108	0.18934	0.0124	0.000381
	R1 ($\Omega.cm^2$)	42040	4048	2334	4.486	1.8522
	R2 ($\Omega.cm^2$)	415.8	36.34	6.19	0.399	0.1723
	R3 ($\Omega.cm^2$)	576.8	60.02	9.802	1.0992	0.1323
	R4 ($\Omega.cm^2$)	3964	-	-	425.2	393
	ASR ($\Omega.cm^2$)	4.69×10^4	4144	2349.9	431.18	395.15
O10	*Lb* (H)	1.07×10^{-4}	1.50×10^{-8}	5.10×10^{-6}	7.77×10^{-11}	2.23×10^{-10}
	Rb ($\Omega.cm^2$)	1.0722	0.5108	0.18934	0.0124	0.000381
	R1 ($\Omega.cm^2$)	42040	4042	2312	4.354	1.8304
	R2 ($\Omega.cm^2$)	415.2	36.32	6.158	0.3152	0.1464
	R3 ($\Omega.cm^2$)	576.4	60.02	9.77	0.6538	0.00085
	R4 ($\Omega.cm^2$)	1884	-	-	424.4	363.4
	ASR ($\Omega.cm^2$)	4.48×10^4	4138.3	2327.92	429.72	365.37
O15	*Lb* (H)	8.33×10^{-5}	5.47×10^{-9}	4.10×10^{-6}	6.22×10^{-13}	5.03×10^{-9}
	Rb ($\Omega.cm^2$)	1.0722	0.5108	0.18934	0.0124	0.000381
	R1 ($\Omega.cm^2$)	42040	4042	2312	4.344	1.8206
	R2 ($\Omega.cm^2$)	413.2	36.22	6.106	0.3048	0.1403
	R3 ($\Omega.cm^2$)	524.4	59.88	9.756	0.6148	0.00031
	R4 ($\Omega.cm^2$)	581.4	-	-	415.8	363.4
	ASR ($\Omega.cm^2$)	4.35×10^4	4138.1	2327.86	421.06	365.36
O25	*Lb* (H)	8.35×10^{-9}	2.48×10^{-9}	4.59×10^{-6}	1.83×10^{-11}	5.92×10^{-8}
	Rb ($\Omega.cm^2$)	1.0722	0.5108	0.18934	0.0124	0.000381
	R1 ($\Omega.cm^2$)	42040	4002	2312	4.306	1.8028
	R2 ($\Omega.cm^2$)	164.18	36.22	6.002	0.241	0.1178
	R3 ($\Omega.cm^2$)	225.2	59.7	9.682	0.3094	0.000147
	R4 ($\Omega.cm^2$)	578.4	-	-	415.8	342.6
	ASR ($\Omega.cm^2$)	4.29×10^4	4097.92	2327.86	420.65	344.52

measured polarization resistance reflects the sum of the polarization resistance of the two electrodes investigated. Thus, all the cell impedances were normalized by the superficial area ($0.04\ cm^2$), so the R parameters obtained in the fitting for each process were divided by two to consider the contribution of the two electrodes.

The n value gives information about the species involved in the electrode reaction (Figure 6). The overall ORR can be summarized as $^1/_2O_2\,(g) + 2e^- \rightarrow O^2$. It is a complex multistep process, which practically involves the gas diffusion, surface adsorption/dissociation, and charge transfer reaction.

It is well known that different processes for oxygen reduction over MIEC electrodes have different relationships with the oxygen partial pressure. The most commonly used parameter to determine the rate-determining step in ORR is n, which indicates the relation between the electrode resistance and oxygen partial pressure,[56] as expressed by following formulae:

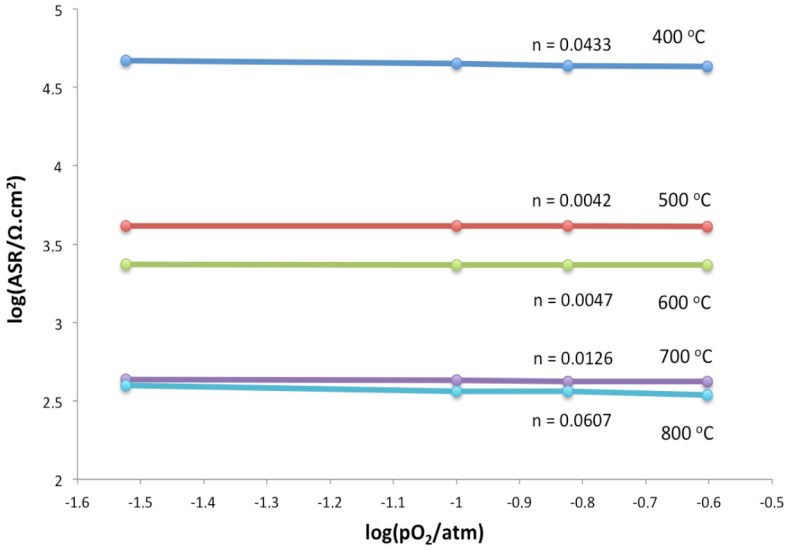

Figure 6. The dependence of the ASR of the LV05SM/YSZ interface as a function of oxygen partial pressure at different temperatures.

$$R = R^o(pO_2)^n,$$

$$n = 1,\ O_2\,(g) \leftrightarrow O_{2,ads},$$

$$n = {}^1\!/_2, O_{2,ads} \leftrightarrow 2O_{ads},$$

$$n = {}^3\!/_8, O_{TPB} + e^- \leftrightarrow O_{TPB},$$

$$n = {}^1\!/_4, O_{ads} + 2e^- + V_{\ddot{O}} \leftrightarrow O_O^x,$$

$$n = {}^1\!/_8, O_{TPB} + e^- \leftrightarrow O_{TPB}^2,$$

$$n = {}^1\!/_{10}, O_{TPB}^2 + V_{\ddot{O}} \leftrightarrow O_O^x.$$

For metal oxides with solid electrolytes, $n = 1$ can be attributed to the gaseous diffusions and adsorptions of oxygen molecules as a limiting step; $n = 1/2$ corresponded to the oxygen adsorption-desorption process, involving oxygen diffusion at the interface of the gas/cathode and surface diffusion of related intermediate oxygen species as a limiting step; $n = 3/8$ was interpreted as a reaction controlled by the atomic oxygen diffusion process (along the two-phase electrode/electrolyte contact), followed by a charge transfer as a limiting step; $n = 1/4$ was related to the charge transfer process on the electrode, occurring at the interfaces of the current collector/electrode and the electrode/electrolyte as a limiting step; $n = 1/8$ was referred to the formation of oxide ions forming the intermediate species as a limiting step; $n = 1/10$ or $n = 0$ can been attributed to the oxygen ion diffusion from the TPB to the electrolyte, respectively. Representative profiles for PO_2 dependence of R_1, R_2, R_3, and $R_2 + R_3$ are shown in Supplementary materials section and the fitting results at various temperatures are listed in Table 2.

From the fitted data values, R_1 is independent of the oxygen partial pressure and R_2 and R_3 increase with decreasing PO_2. It is clearly observed that R_1 did not have a monotonic dependence on oxygen partial pressure. The resistance of the high-frequency arc decreases with increasing temperatures, and it is independent

of the oxygen partial pressure. The oxygen partial pressure dependence was calculated as $n = 0$. These results indicate that this process is related neither to charge transfer nor to diffusion processes. Therefore, the first arc could be caused by the oxygen ions transferring through the electrolyte/electrode interface. The polarization resistances R_2 and R_3, associated with Arc2 and Arc3 appearing at intermediate-frequency ranges, are found to be highly dependent on the oxygen partial pressure. Both R_2 and R_3 decreased with increased oxygen partial pressure and increased temperature. The values obtained for n are 0.017–0.221 for R_2 and 0.0023–0.54 for R_3 at the investigated temperatures. Considering the low oxygen partial pressure, this process could be related to an oxygen atom diffusion followed by a charge transfer.

The process associated with the low-frequency arc presents the lowest impedance values. $R_2 + R_3$ was found to be dependent on PO_2 with values of $n = 0.021$–0.4321. It suggests that both R_2 and R_3 are associated with electron transfer. In other words, the electron transfer process may be composed of two successive intermediate steps, showing similar importance in the charge transfer process. The polarization resistance of this process quickly reduced with increasing oxygen partial pressure, which is in agreement with the behavior of a gas diffusion process. An increase of oxygen partial pressure results in a sufficient supply of oxygen to the electrode from the gas phase, thereby effectively eliminating diffusion polarization resistance.

The ASR values for ORR are obtained by the sum of individual resistances associated with each process. As expected, the ASR for the LV05SM/YSZ interface decreases notably with increasing temperature and slightly with the oxygen partial pressure, as shown in Figure 6. The characteristic of ASR shows a quite weak PO_2 dependency ($n = 0.0042$–0.0607), which could be related to the oxide ion transfer within the bulk electrode and/or from the electrode to YSZ electrolyte through the TPB. Therefore, this process is the major rate-limiting step for the LV05SM cathode.

EIS data show the impedance responses for the single-phase LV05SM electrode on the GDC electrolyte as measured under different oxygen partial pressures and collected every 50 °C in the temperature range from 400 to 800 °C.

From the detailed analysis (given in Supplementary materials), it can be concluded that the EIS diagrams are composed of arcs located in high- and low-frequency zones. This indicates that at least two different steps are involved in the ORR over the electrode. It is clearly seen that below 700 °C, two well-separated semicircles are observed in the high-frequency part of the Nyquist plots. With increasing operating temperature, the high-frequency arc size decreased noticeably, and it totally disappeared at 700 °C and higher. The impedances of a symmetric cell may arise from both the electrodes and electrolyte. The electrolyte typically performs as an ideal resistor, which represents the intercept value in the impedance diagram at the high-frequency side with the real axis and corresponds to the electrolyte resistance, electrode ohmic resistance, and lead resistance. With the decrease in operation temperature, a semicircle associated with the oxide ion diffusion around the grain boundary of the electrolyte appeared in the high-frequency range.

EIS data also illustrate the impedance diagrams measured at 600 °C under different oxygen partial pressures. Three arcs at high, medium, and low frequencies can be observed. In general, the high- and medium-frequency arcs show little dependence on the oxygen partial pressure, while the amplitude of the low-frequency arc increases slightly as oxygen partial pressure decreases. The magnitude of arcs changes significantly with the temperature (given in Supplementary materials). In order to determine the processes involved in the ORR, the effect of oxygen partial pressure in the electrode impedance as a function of temperature was further studied. The oxygen partial pressure was varied between 0.01 and 0.25 atm by mixing O_2 with N_2 using mass flow controllers.

The typical complex EIS plots between 400 and 800 °C in air at 3% – 10% – 15% – 25% O_2 for the LV05SM cathode with GDC electrolyte are depicted in Figure 7. Two visible semicircular arcs in the complex impedance plots are observed.

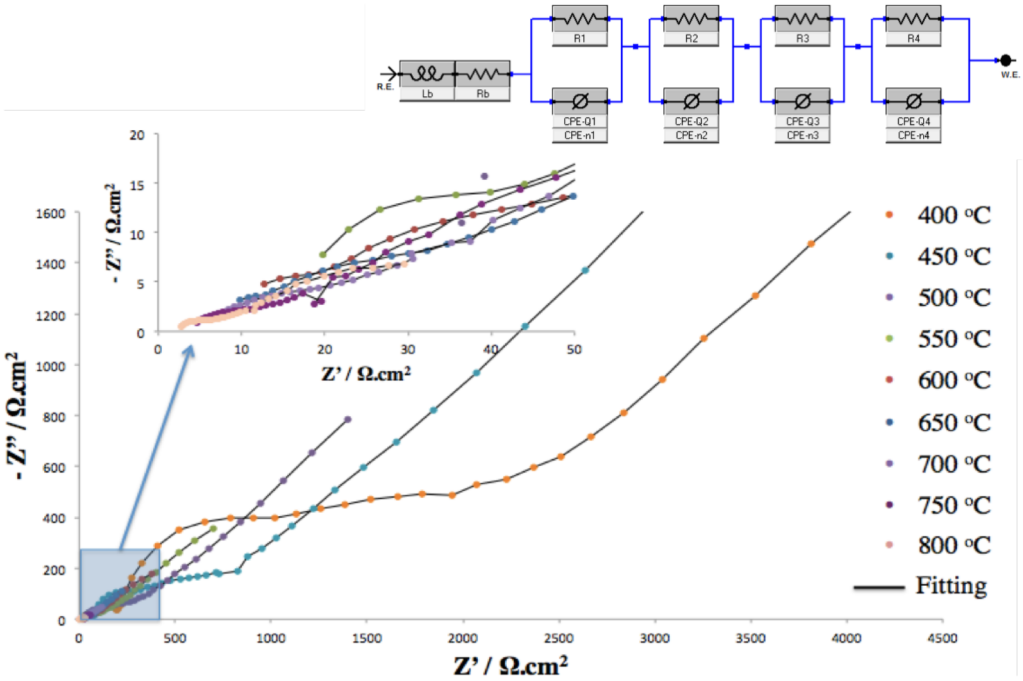

Figure 7. Experimental and fit Nyquist plots for a symmetrical LV05SM/GDC/LV05SM cell measured at 25% O_2 and 75% N_2 between 400 and 800 °C.

Similar trends of the complex impedance diagrams were observed. Indeed, several intermediate steps are involved during the overall ORR process. These steps may occur simultaneously on different time scales, which contributes significantly to total electrode polarization resistance R_p. However, the entire frequency response can accurately be described by a medium-frequency depressed semicircle and a low-frequency skewed semicircular arc. The presence of two semicircular arcs in the complex impedance plane suggests that the ORR over the electrode was composed of at least two distinct processes. The overall size of the two arcs is generally attributed to R_p. However, with the decrease in operation temperature, a semicircle associated with the migration of oxide ions through the grain boundary of the GDC electrolyte also appeared in the high-frequency range.[57]

The experimental impedance spectra, simulated response, and electrical equivalent circuit models are shown in Figure 7. The simulated curve (solid line obtained from the electrical equivalent model) fits well with the experimental data. In fact, fewer electrical circuits were considered while obtaining the most accurate fit for the measured data. Customarily, the complex impedance response of a symmetric cell is modeled using the equivalent circuit of $L--R_b--(R_1 - QPE_1)--(R_2 - QPE_2)...(R_i - QPE_i)$ shown in Figure 7's inset by means of Gamry software. The data fitting reveals three processes in the electrode reaction. In the high-frequency range serial inductance L was included to simulate the inductive effects of the setup at high frequencies. A serial R_b was used to simulate the grain boundary contributions of the GDC electrolyte at low temperatures and RQ elements were fitted as each one being assigned to a specific electrochemical phenomenon. The exact equivalent circuits adopted for fitting the EIS data at temperatures of 400–500 °C are fitted well to

an equivalent circuit of $L--R_b--(R_1 - QPE_1)--(R_2 - QPE_2)--(R_3 - QPE_3)--(R_4 - QPE_4)$ and the temperatures between 600, 700, and 800 °C are fitted well to an equivalent circuit of $L--R_b--(R_1 - QPE_1)--(R_2 - QPE_2)--(R_3 - QPE_3)$. The first component $(R_1\,QPE_1)$ represents the semicircle in the high-frequency region, the second one $(R_2\,QPE_2)$ a semicircle in the medium-frequency region, and the third one $(R_3\,QPE_3)$ a semicircle in the low-frequency region.

The size of the high-frequency arc decreased as the operation temperature decreased and it totally disappeared above 700 °C. This signifies that the high frequency arc at 400– 600 °C can be attributed to the migration of oxide ions through the GDC electrolyte. The oxygen reduction over the LV05SM electrode is responsible for the second semicircle in the EIS data. Impedance at high and intermediate frequencies is related to ion and electron transfer at the electrode, electrolyte, and collector/electrode interfaces, while the impedance at low frequencies is associated with noncharge transfer, such as oxygen surface exchange and gas-phase diffusion inside and outside the electrode layer.[55]

Table 3 summarizes the fitted parameters as a function of temperature for LV05SM/GDC/LV05SM under different partial pressure of oxygen, as well as the ASR values. The inductance value was shown but not considered in the present study. It can be seen that the electrolyte resistance (R_b) as well as the four resistances (R_1, R_2, R_3, R_4) associated with the kinetics of electrode processes decrease with increasing temperature, as expected. It also can be seen that the electrolyte resistance, R_b, does not depend on the oxygen partial pressure, remaining stable at each temperature, which is in agreement with the behavior of a pure ionic conductor such as the GDC electrolyte. The expected but invisible right intercept on the real axis in the EIS diagram represents the total resistance (R_{tot}) and the left intercept on the real axis corresponds to the ohmic resistance (R_{ohm}, including the electrolyte and connection wires). The polarization resistance (R_p) is estimated from the difference between R_{tot} and R_{ohm} $(R_p = R_{tot} - R_{ohm})$. Thus, all the cell impedances were normalized by the superficial area (0.04 cm^2), so the R parameters obtained in the fitting for each process were divided by two to consider the contribution of the two symmetric electrodes.

The most commonly used parameter to determine the rate-determining step in the ORR is the slope of the electrode resistance as a function of oxygen partial pressure. The parameter called n gives information about the species involved in the electrode reaction in Figure 6 mentioned above. The overall ORR can be simply described as $^1/_2O_2\,(g) + 2e \rightarrow O^2$. In reality, it may involve many substeps such as gas diffusion, surface adsorption, dissociation, electron and ion charge transfer, etc.[58] In order to operate a cell in the intermediate-temperature range, it is of vital importance to accelerate the ORR in the cathode and the oxygen transport in the cathode and electrolyte. Representative profiles for PO_2 dependence of R_1, R_2, R_3, and $R_2 + R_3$ are shown in Figure 7 and the fitting results at various temperatures are listed in Table 3. From the fitted data values, R_1 is slightly dependent on the oxygen partial pressure and R_2 and R_3 increase with decreasing PO_2. It is clear that R_1 did not have a monotonic dependence on PO_2. The resistance of the high-frequency arc decreases with increasing temperatures, and it is independent of the oxygen partial pressure. Therefore, the first arc could be caused by the oxygen ions transferring through the electrolyte/electrode interface.

The polarization resistances R_2 and R_3, associated with Arc2 and Arc3 appearing at intermediate-frequency ranges, are found to be dependent on PO_2. Both R_2 and R_3 decreased with increase in PO_2 and increase in temperature. The values obtained for n are 0.0091–0.2067 for R_2 and 0.0033–0.1434 for R_3 at the investigated temperatures. Considering the weak oxygen partial pressure, this process could be related to oxygen atom diffusion followed by a charge transfer.

Table 3. The fitted parameters as a function of temperature for LV05SM/GDC/LV05SM in PO_2.

PO_2	T (°C)	400	500	600	700	800
O3	*Lb* (H)	1.38×10^{-9}	1.92×10^{-9}	1.13×10^{-9}	1.44×10^{-7}	6.47×10^{-7}
	Rb ($\Omega.cm^2$)	81.52	15.974	0.8132	0.8096	0.7536
	R1 ($\Omega.cm^2$)	7126	7064	907	228.6	13.542
	R2 ($\Omega.cm^2$)	335.2	25.14	5.926	1.3986	1.125
	R3 ($\Omega.cm^2$)	1864.4	130.66	92.96	16.646	7.04
	R4 ($\Omega.cm^2$)	252.2	85.02	-	-	-
	ASR($\Omega.cm^2$)	9577.8	7304.82	1005.88	246.64	21.707
O10	*Lb* (H)	1.54×10^{-9}	8.39×10^{-10}	2.91×10^{-10}	3.83×10^{-7}	8.51×10^{-7}
	Rb ($\Omega.cm^2$)	81.52	15.974	0.8132	0.8096	0.7536
	R1 ($\Omega.cm^2$)	7126	6318	907	228.6	13.54
	R2 ($\Omega.cm^2$)	316.6	25.14	4.074	1.3304	1.1238
	R3 ($\Omega.cm^2$)	1793.4	100.52	92.6	16.646	7.04
	R4 ($\Omega.cm^2$)	252.2	82.62	-	-	-
	ASR ($\Omega.cm^2$)	9488.2	6526.28	1003.67	246.57	21.70
O15	*Lb* (H)	2.88×10^{-9}	1.75×10^{-8}	5.33×10^{-11}	2.82×10^{-7}	7.76×10^{-7}
	Rb ($\Omega.cm^2$)	81.52	15.974	0.8132	0.8096	0.7536
	R1 ($\Omega.cm^2$)	7126	6318	905.8	228.6	12.732
	R2 ($\Omega.cm^2$)	315.8	24.8	3.94	1.3304	1.1086
	R3 ($\Omega.cm^2$)	1782	99.56	92.36	16.328	6.946
	R4 ($\Omega.cm^2$)	252.2	82.62	-	-	-
	ASR($\Omega.cm^2$)	9476	6524.98	1002.1	246.26	20.78
O25	*Lb* (H)	2.49×10^{-9}	1.52×10^{-8}	4.74×10^{-8}	3.86×10^{-7}	7.31×10^{-7}
	Rb ($\Omega.cm^2$)	81.52	15.974	0.8132	0.8096	0.7536
	R1 ($\Omega.cm^2$)	7126	5184	905	228.6	12.732
	R2 ($\Omega.cm^2$)	315.8	24.14	3.94	1.1038	1.1038
	R3 ($\Omega.cm^2$)	1782	97.8	92.36	16.28	6.946
	R4 ($\Omega.cm^2$)	252.2	82.62	-	-	-
	ASR ($\Omega.cm^2$)	9476	5388.56	1001.3	245.98	20.78

The process associated with the low-frequency arc presents $R_2 + R_3$, which was found to be dependent on PO_2 with values of n = 0.0072–0.1297. It suggests that both R_2 and R_3 are associated with electron transfer. In other words, the electron transfer process may be composed of two successive intermediate steps, showing comparable importance in the charge transfer process. An increase in PO_2 results in a sufficient supply of O_2 to the electrode from the gas phase, effectively eliminating diffusion polarization resistance.

The ASR values for ORR are obtained by the sum of individual resistances associated with each process. As expected, the ASR for the LV05SM/GDC interface decreases notably with increasing temperature and slightly with the oxygen partial pressure as shown in Figure 8. The characteristic of ASR shows quite weak PO_2 dependency (n = 0.0012–0.1261), which could be related to the oxide ion transfer within the bulk electrode and/or from electrode to electrolyte through the TPB. Therefore, this process is the major rate-limiting step for LV05SM cathode.

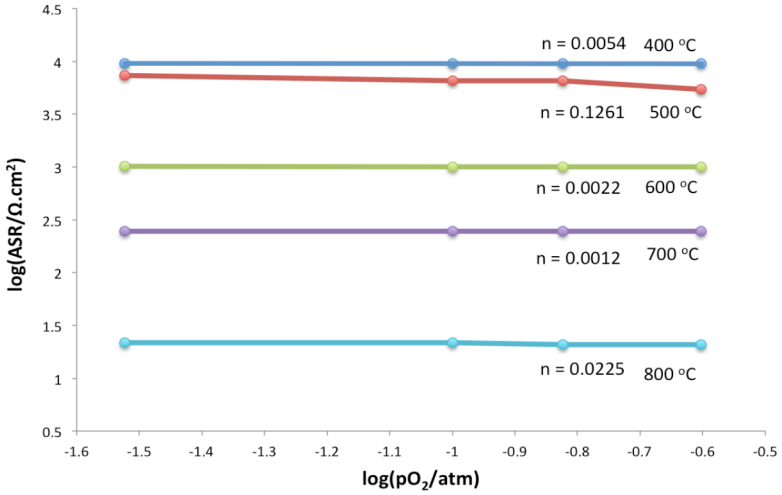

Figure 8. The dependence of the ASR of the LV05SM/GDC interface as a function of PO_2 at different temperatures.

In conclusion, $V^{4+/5+}$ cation-doped LSM ($La_{0.6-x}V_xSr_{0.4}MnO_{3-\delta}$, $x = 0.005 - 0.1$) cathode materials were synthesized for the first time by sol-gel method and characterized by XRD, XPS, and SEM. The XRD patterns show a single-phase perovskite structure for the LV05SM sample and the relative peaks were sharp, indicating good incorporation into the lattice of the metal oxides used in the powder synthesis. The valance states of the elements in the possession and the composition of the surface of the LV05SM cathode sample are proven by XPS without any impurities. By replacing La atoms with V atoms, the ionic conductivity and catalytic activity of the LV05SM material and hence the performance of the cathode material are enhanced due to multiple stable oxidation states of V atoms such as $+4$ and $+5$. The SEM images of the surface and cross-section of the LV05SM symmetric cell suggested good adhesion between electrode and electrolyte layers. As seen from the images, grains in the electrode and electrolyte have good contact and pores are uniformly distributed in the cathode. Electrical conductivity values for LV05SM are 5%–10% higher than those of conventional LSM cathode material at lower temperatures.

EIS was performed under reducing atmospheres, using a symmetric cell configuration, (cathode/electrolyte/cathode), with YSZ and GDC as electrolytes. Better ASR values were obtained, suggesting that LV05SM shows better performance compared to conventional LSM cathode materials. Three main electrochemical trends are investigated in EIS data, corresponding to the oxygen ion incorporation, surface diffusion of oxygen species, and oxygen adsorption and dissociation. By using fitting models and investigating the trends it is concluded that oxide ion transfer within the bulk electrode and/or from the electrode to the YSZ/GDC electrolyte through the TPB is the limiting step in the ORR mechanism in the intermediate temperature range (400–700 °C). From the EIS data, we conclude that doping of V^{4+} and V^{5+} ions enhances the performance of the cathode.

All of the abovementioned results summarize that LV05SM is a promising cathode. In particular, the $La_{0.595}V_{0.005}Sr_{0.4}MnO_{3-\delta}$ cathode with good electrocatalytic activity for ORR can be considered as a potential cathode material for IT-SOFC applications.

3. Experimental

3.1. Preparations and characterizations of cathode materials

The $La_{0.6-x}V_xSr_{0.4}MnO_{3-\delta}$ (LVxSM, x = 0.005 – 0.1) powders were synthesized through a sol-gel technique. Figure 9 shows the flow sheet for the preparation of LVxSM cathode powders by sol-gel process. La, Sr, and Mn nitrates and V acetate (purity >99.9%, Aldrich Chemicals, USA) were used as reagents.

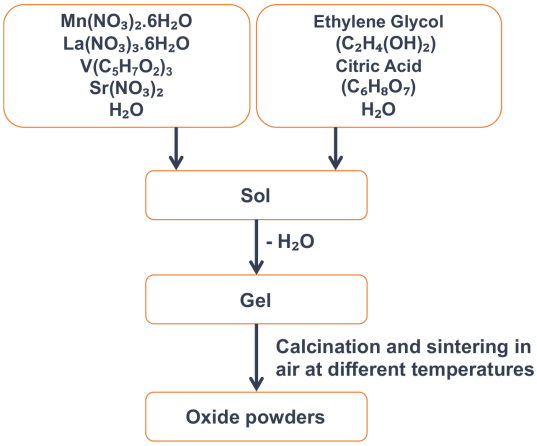

Figure 9. Flow sheets for the preparation of $La_{0.595}V_{0.005}Sr_{0.4}MnO_{3-\delta}$ cathode powders by sol-gel process.

All of the reagents in requisite stoichiometric ratios were dissolved in distilled deionized water separately. Thereafter, all the solutions were mixed together and stirred to obtain a homogeneous solution. After their complete dissolution, certain amounts of citric acid and ethylene glycol were introduced as polymerization and complexation agents, respectively.

The mole ratio of citric acid/total metal ions was kept as 1:2:1. The solution was evaporated on a hotplate using a magnetic stirrer until a chocolate-colored gel was formed. When the heating was continued further, the gel completely burned to yield a light and fragile ash. After this mild heating induced gelation, the resulting gel was held in a drying oven at 400 °C for 2 h to remove organics and sintered at 900 and 1100 °C for 3 h to obtain the perovskite compounds with sufficient crystallinity, as confirmed by XRD analysis. The powder XRD data (crystal structure and phase composition of the synthesized powders) were collected on a Rigaku D/MAX-Ultima+/PC Diffractometer using Cu-Kα radiation (λ = 1.54056 A§). The data obtained were compared with reference data for identification of the crystal structure. The morphology of the surface and the cross-sections of the sintered symmetric cells were examined by scanning electron microscope (ESEM-FEG, Philips XL 30) at an accelerating potential of 10 kV.

The XPS experiments were performed using a Thermo Scientific K-Alpha Surface Analysis instrument at room temperature. An Al K Alpha X-ray source was used with a spot size of 400 µm and the spectra of powdered samples were recorded with constant pass energy values at 150 eV. The energy step size was set as 0.100 eV and the charge effect was calibrated using the binding energy of C1s (284.5 eV).

3.2. Symmetric cell fabrication for electrochemical impedance analysis

Symmetrical electrochemical cells for impedance studies were prepared using LV05SM cathode material and YSZ electrolyte. The electrolyte pellets were prepared by pressing commercial powders in a cylindrical stainless-steel mold (5 mm in diameter and a thickness of about 0.5 mm) with a uniaxial dry press at a pressure of 400 MPa. After that, the prepared electrolyte disks were initially calcined at 400 °C for 2 h, followed by sintering at 1300 °C for 2 h. For symmetrical cells, cathode samples were mixed thoroughly with organic binder (polyvinyl butyral) to make the cathode slurry. The paste obtained was painted on both sides of the pellets with dimensions of 2 × 2 mm by using masking tape. The symmetrical cell was then dried at 150 °C for 1 h and sintered at 1300 °C for 1 h in air to form porous electrodes well adhered to the electrolytes. The final active area of each cathode

was about 0.04 cm^2. Finally, the cathodes were connected with Au paint and wire as currents collectors. The symmetrical cells were assembled into a lab-designed setup that allowed performing the experiments in different atmospheres. To determine the resistance of the various cathode processes, the manufactured symmetric cells were characterized by EIS measurements in ambient air from 400 to 700 °C with an increment of 50 °C. The O_2 concentrations (% O_2) around the cell during the measurements were maintained using electronic mass flow controllers and nitrogen was used as the carrier gas. Impedance spectra were measured in the frequency range of 0.1 Hz to 1 MHz with 10 mV amplitude of the AC signal. The spectra were analyzed using the Gamry Interface 1000 Potentiostat/Galvanostat, which was interfaced with a computer-controlled program for data acquisition.

3.3. Electrical conductivity measurements

Electrical conductivity was measured as a function of temperature by the standard DC four-terminal method. The conductivity measurements were performed in air on sintered rectangular bars of approximate dimensions 20 × 5 × 2 mm. Electrical contacts using Au wires (0.25 mm in diameter, Alfa Aesar) and Au conductor paste (Heraeus) were placed onto the edges of the sample ensuring a homogeneous current flow. Voltage contacts were prepared as small as possible to prevent any disturbance of the contacts on the current flow. Measurements were performed from 400 to 800 °C with an interval of 50 °C. The conductivity (σ) was determined from a set of V – I values by taking $\sigma = \frac{1}{\rho} = \frac{L}{A} \times \frac{dI}{dV}$, where L is the distance between voltage contacts and A is the sample cross-section.

Acknowledgment

The authors gratefully acknowledge the financial grants supplied by the Scientific and Technological Research Council of Turkey (TÜBİTAK) (Project No: 112M279 and 214Z094) and Boğaziçi University, Scientific Research Projects (BAP) (Project No: 5341 - 10B05S11).

References

1. Skinner, S. J.; Lashtabeg, A. *J. Mater. Chem.* **2006**, *16*, 3161-3170.
2. Winter, M.; Brodd, R. J. *Chem. Rev.* **2004**, *104*, 4245-4270.
3. Ormerod, R. M. *Chem. Soc. Rev.* **2003**, *32*, 17-28.
4. Choudhury, A.; Chandra, H.; Arora, A. *Renew. Sust. Energ. Rev.* **2013**, *20*, 430-442.
5. Sammes, N. M.; Bove, R.; Pusz, J. *Solid Oxide Fuel Cells*; Springer: London, UK, 2006.
6. Yamamoto, O. *Electrochim. Acta* **2000**, *45*, 2423-2435.
7. Wachsman, E. D.; Lee, K. T. *Science* **2011**, *334*, 935-939.
8. Brett, D. J. L.; Atkinson, A.; Brandon, N. P.; Skinner, S. J. *Chem. Soc. Rev.* **2008**, *37*, 1568-1578.
9. Istomin, S. Y.; Antipov, E. V. *Russ. Chem. Rev.* **2013**, *82*, 686.
10. Tsipis, E. V.; Kharton, V. *J. Solid State Electrochem.* **2008**, *12*, 1367-1391.
11. Sun, C.; Hui, R.; Roller, J. *J. Solid State Electrochem.* **2010**, *14*, 1125-1144.
12. Nakamura, A.; Inami, T.; Shimojo, Y.; Morii, Y. *J. Solid State Chem.* **1998**, *141*, 404-410.
13. Sengodan, S.; Choi, S.; Jun, A. *Nat. Mater.* **2015**, *14*, 205-209.
14. Carpanese, M. P.; Clematis, D.; Bertei, A.; Giuliano, A. *Solid State Ionics* **2017**, *301*, 106-115.

15. Mizusaki, J.; Mori, N.; Takai, H.; Yonemura, Y.; Minamiue, H.; Tagawa, H.; Dokiya, M.; Inaba, H.; Naraya, K.; Sasamoto, T. et al. *Solid State Ionics* **2000**, *129*, 164-177.
16. De Souza, R. A.; Kilner, J. A.; Walker, J. F. *Mater. Lett.* **2000**, *43*, 43-52.
17. Chen, Y.; Shen, J.; Yang, G.; Zhou, W.; Shao, Z. *J. Mater. Chem.* **2017**, *5*, 24842-24849.
18. Magee, J. S.; Mitchel, M. M. *Stud. Surf. Sci. Catal.* **1993**, *76*, 105.
19. Burns, R. G. *Mineralogical Applications of Crystal Field Theory*; Cambridge University Press: Cambridge, UK, 1993.
20. Baltes, M. PhD, University of Antwerp, Antwerp, Belgium, 2001.
21. Trifiro, F.; Grzybowska, B. *Appl. Catal. A Gen.* **1997**, *157*, 1-425.
22. Bond, G. C.; Tahir, S. F. *Appl. Catal.* **1991**, *71*, 1-31.
23. Deo, G.; Wachs, I. E.; Haber, J. *Crit. Rev. Surf. Chem.* **1994**, *4*, 141.
24. Ertl, G.; Knozinger, H.; Weitkamp, J. *Handbook of Heterogeneous Catalysis*; Wiley: Weinheim, Germany, 1997.
25. Thomas, J. M.; Thomas, W. J. *Principles and Practice of Heterogeneous Catalysis*; Wiley: Weinheim, Germany, 1997.
26. Hagen, J. *Industrial Catalysis, A Practical Approach*; Wiley: Weinheim, Germany, 1999.
27. Rase, H. F. *Handbook of Commercial Catalysts*; CRC Press: New York, NY, USA, 2000.
28. Yang, T. C. K., Lang, Y.; Juang, R.; Chiu, T.; Chen, C. *Vacuum* **2015**, *121*, 310-316.
29. Kamata, H.; Takahashi, K.; Odenbrand, C. U. I. *J. Catal.* **1999**, *185*, 106-113.
30. Cao, X. G.; Jiang, S. P. *Int. J. Hydrogen Energ.* **2013**, *38*, 2421-2431.
31. Chiba, R.; Yoshimura, F.; Sakurai, Y. *Solid State Ionics* **1999**, *124*, 281-288.
32. Gunasekaran, N.; Bakshi, N.; Alcock, C. B.; Carberry, J. J. *Solid State Ionics* **1996**, *83*, 145-150.
33. Nefzi, H.; Sediri, F. *J. Solid State Chem.* **2013**, *201*, 237-243.
34. Falcon, H.; Barbero, J. A.; Alonso, J. A.; Martinez-Lope, M. J.; Fierro, J. L. G. *Chem. Mater.* **2002**, *14*, 2325-2333.
35. Shichi, Y.; Inoue, Y.; Munakata, F.; Yamanaka, M. *Phys. Rev. B* **1990**, *42*, 939-942.
36. Wagner, C. D.; Riggs, W. M.; Davis, L. E.; Moulder, J. F.; Muilenberg, G. E. *Handbook of X-Ray Photoelectron Spectroscopy*; PerkinElmer Corporation: Waltham, MA, USA, 1979.
37. Kamata, H.; Yonemura, Y.; Mizusaki, J.; Tagawa, H.; Naraya, K.; Sasamoto, T. *J. Phys. Chem. Solids* **1995**, *56*, 943-950.
38. Dorris, S. E.; Mason, T. O. *J. Am. Ceram. Soc.* **1988**, *71*, 379-385.
39. Raffaelle, R.; Anderson, H. U.; Sparlin, D. M.; Parris, P. E. *Phys. Rev. B* **1991**, *43*, 7991-8000.
40. Zhang, K.; Ran, R.; Ge, L.; Shao, Z.; Jin, W.; Xu, N. *J. Membrane Sci.* **2008**, *323*, 436-443.
41. Zhao, H.; Cheng, Y.; Xu, N.; Li, Y.; Li, F.; Ding, W.; Lu, X. *Solid State Ionics* **2010**, *181*, 354-358.
42. Zhao, H.; Teng, D.; Zhang, X.; Zhang, C.; Li, X. *J. Power Sources* **2009**, *186*, 305-310.
43. Stevesson, J. W.; Armstrong, T. R.; Carneim, R. D.; Pederson, L. R.; Weber, W. J. *J. Electrochem. Soc.* **1996**, *143*, 2722-2729.
44. Wandekar, R. V.; Wani, B. N.; Bharadwaj, S. R. *Solid State Ionics* **2009**, *11*, 240-250.
45. Aruna, S. T.; Muthuraman, M.; Patil, K. C. *J. Mater. Chem.* **1997**, *7*, 2499-2503.
46. Kuharuangronga, S.; Dechakupt, T.; Aungkavattan, P. *Mater. Lett.* **2004**, *58*, 1964-1970.
47. Mizusaki, J.; Yonemura, Y.; Kamata, H.; Ohyama, K.; Mori, N.; Takai, H.; Tagawa, H.; Dokiya, M.; Naraya, K.; Sasamoto, T et al. *Solid State Ionics* **2000,** *132*, 167-180.

48. Yang, C. T.; Wei, W. J.; Roosen, A. *Mater. Chem. Phys.* **2003**, *81*, 134-142.
49. Lee, Y.; Kim, J.; Lee, Y.; Kim, I.; Moon, H. *J. Power Sources* **2003**, *115*, 219-228.
50. Flores, J. C. P.; Coll, D. P.; Martín, S. G.; Ritter, C.; Mather, G. C.; Vazquez, J. C.; Sanchez, M. G.; Alvarado, F. G.; Amador, U. *Chem. Mater.* **2013**, *25*, 2584-2494.
51. Jiang, S. P. *J. Mater. Sci.* **2008**, *43*, 6799-6833.
52. Minh, N. Q.; Takahashi, T. *J. Am. Ceram. Soc.* **1995**, 117-146.
53. De Souza, R. A.; Kilner, J. A. *Solid State Ionics* **1999**, *126*, 153-161.
54. Zhan, Z. L.; Wen, T. L.; Tu, H. Y.; Lu, Z. Y. *J. Electrochem. Soc.* **2001,** *148*, 427-432.
55. Adler, S. B.; Chen, X. Y.; Wilson, J. R. *J. Catal.* **2007**, *245*, 91-109.
56. Escudero, M. J.; Aguadero, A.; Alonso, J. A.; Daza, L. *J. Electroanal. Chem.* **2007**, *611*, 107-116.
57. Chaudhari, V. N.; Khandale, A. P.; Bhoga, S. S. *J. Power Sources* **2014**, *248*, 647-654.
58. Chen, D.; Ran, R.; Zhang, K.; Wang, J.; Shao, Z. *J. Power Sources* **2009**, *188*, 96-105.

Supplementary materials

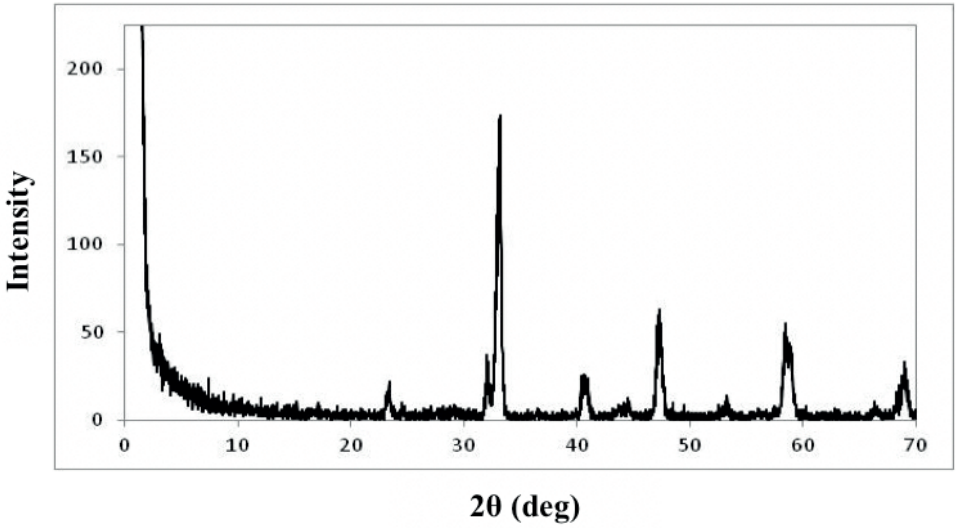

Supplementary Figure 1. XRD data for $La_{0.595}V_{0.005}Sr_{0.4}MnO_{3-\delta}$.

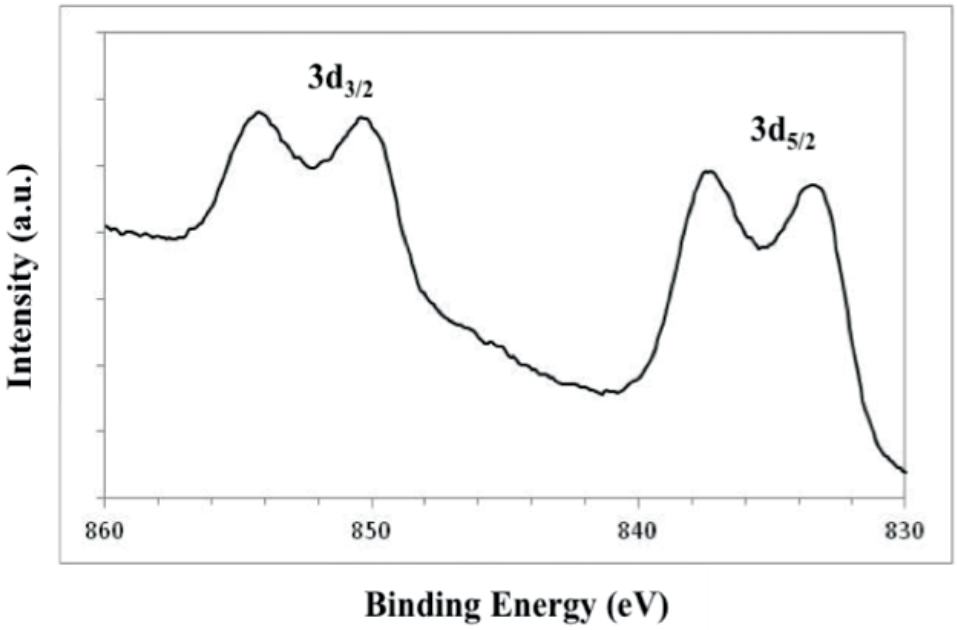

Supplementary Figure 2. XPS spectra of La3d for LV05SM sample.

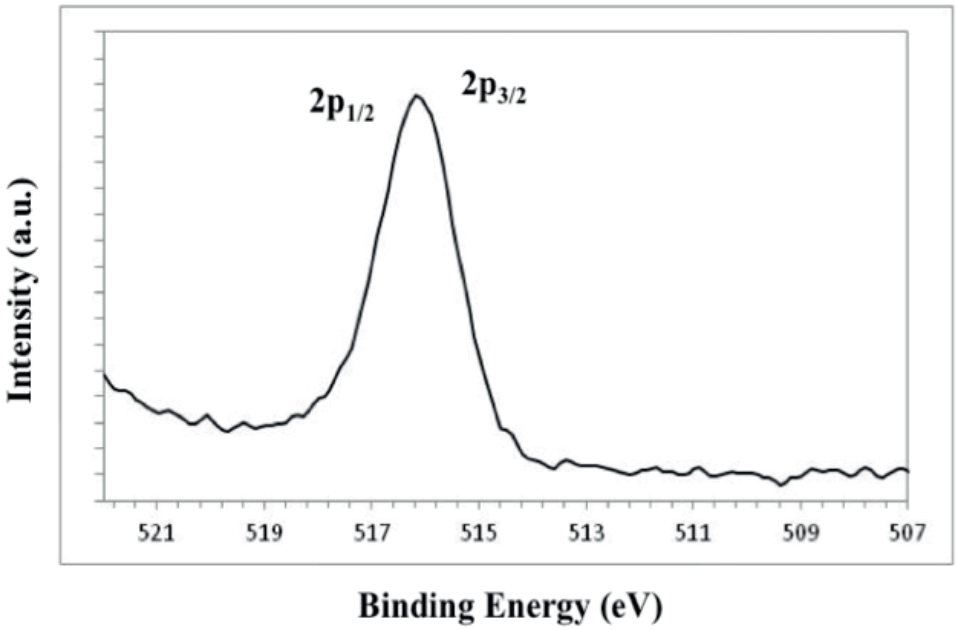

Supplementary Figure 3. XPS spectra of V2p for LV05SM sample.

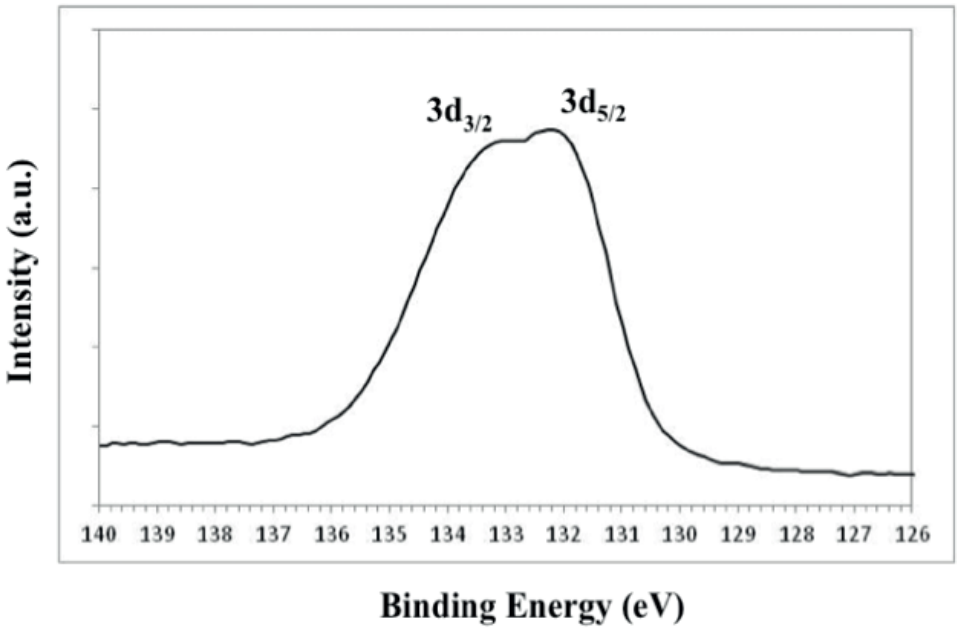

Supplementary Figure 4. XPS spectra of Sr3d for LV05SM sample.

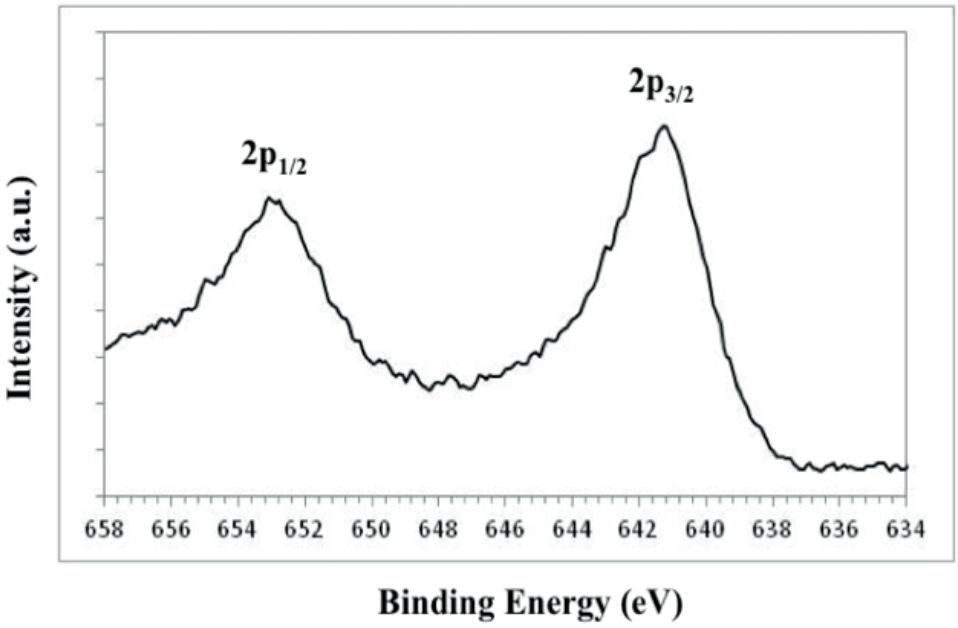

Supplementary Figure 5. XPS spectra of Mn2p for LV05SM sample.

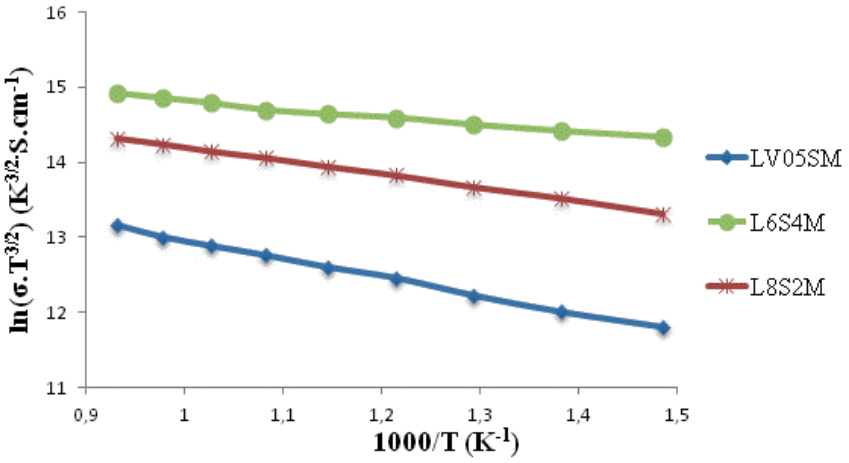

Supplementary Figure 6. Electrical conductivity of $La_{0.595}V_{0.005}Sr_{0.4}MnO_{3-\delta}$ (LV05SM) compared with manganese-containing conventional cathode materials.

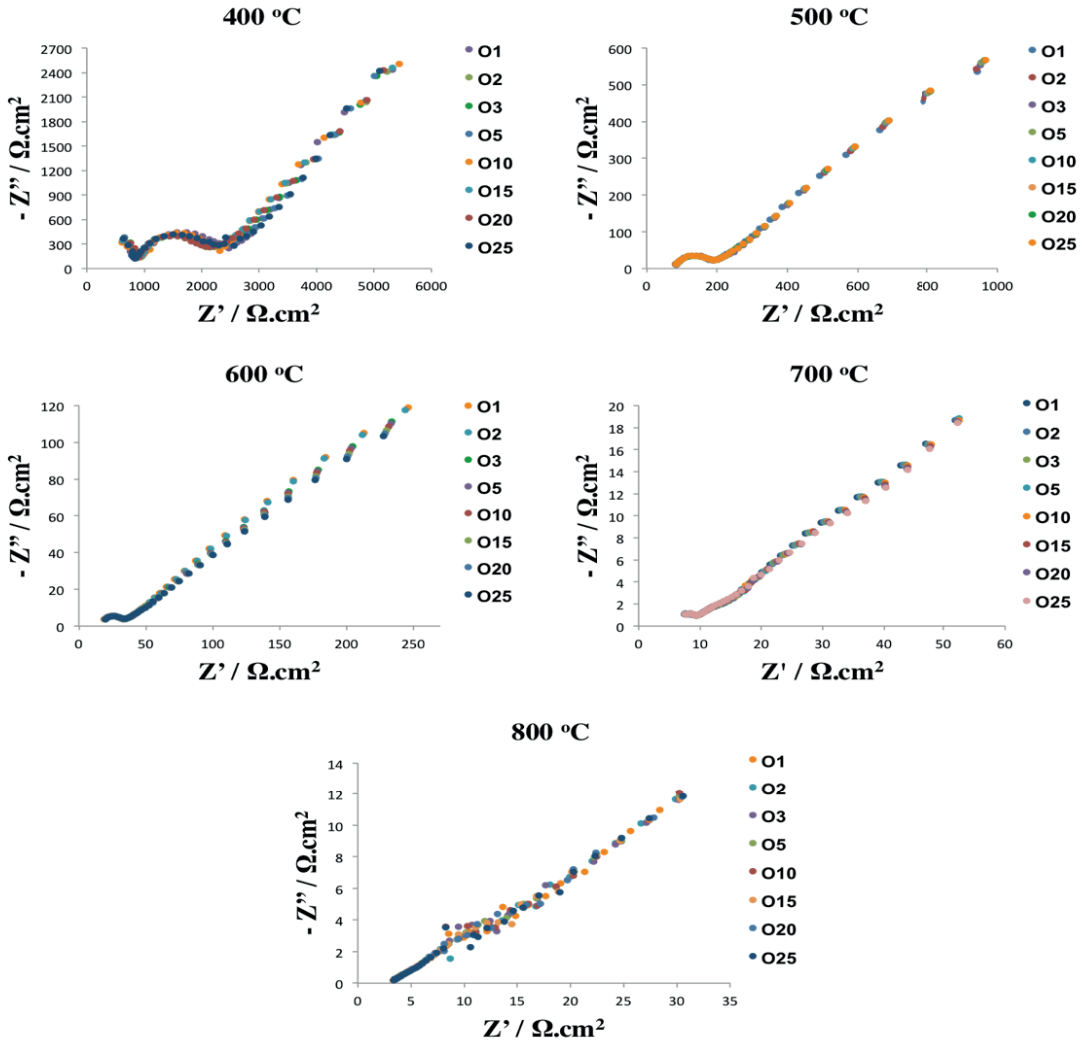

Supplementary Figure 7. Complex impedance plots for LV05SM/YSZ/LV05SM symmetric cell at between 400 and 800 °C for different oxygen partial pressures.

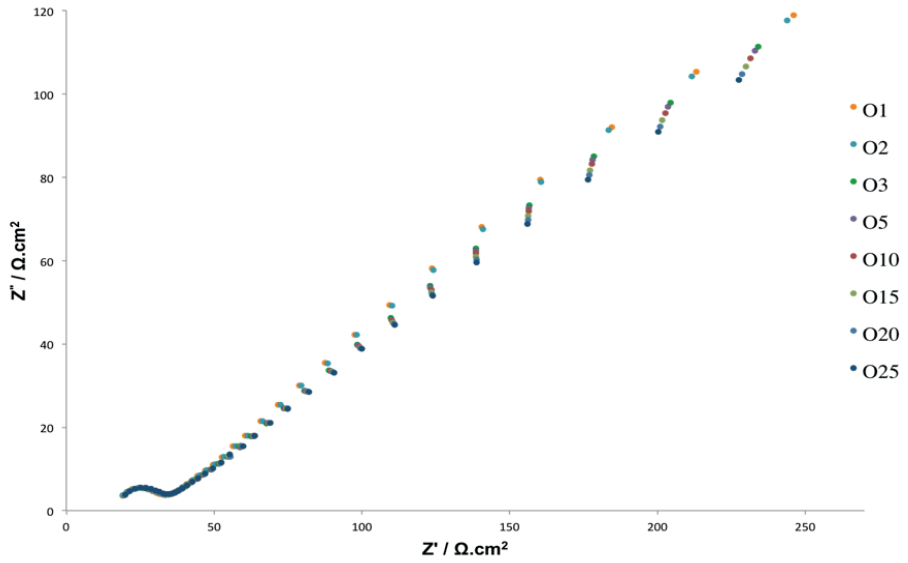

Supplementary Figure 8. Typical EIS of a symmetric LV05SM/YSZ/LV05SM cell measured at 600 °C while fixing the oxygen partial pressure between 1% and 25%.

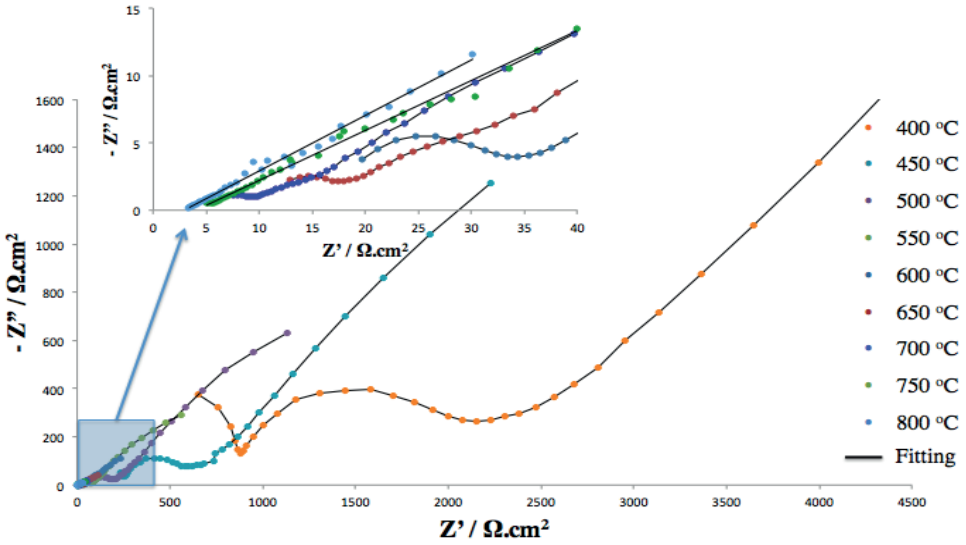

Supplementary Figure 9. Impedance spectra of LV05SM cathode measured in 3% O_2 and 97% N_2 at various temperatures with data fitting.

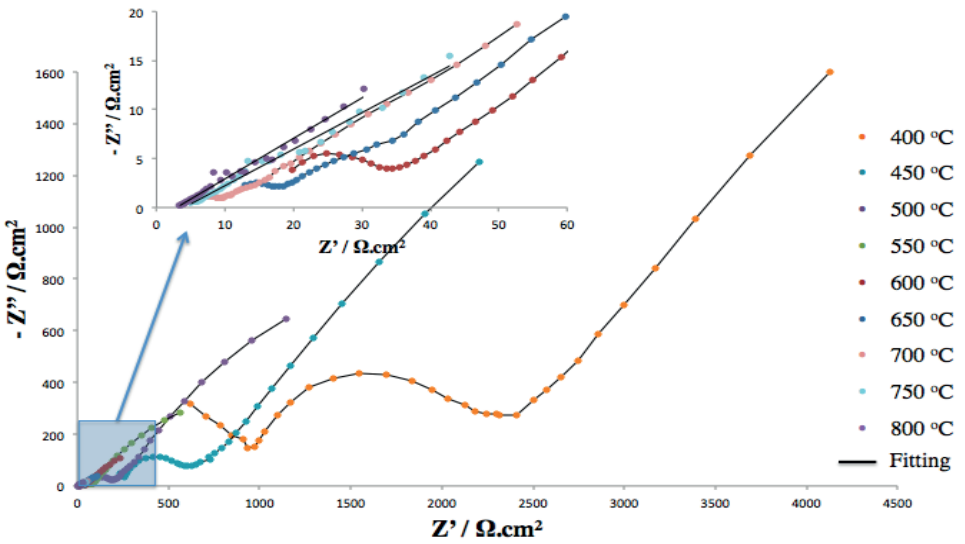

Supplementary Figure 10. Impedance spectra of LV05SM cathode measured in 10% O_2 and 90% N_2 at various temperatures with data fitting.

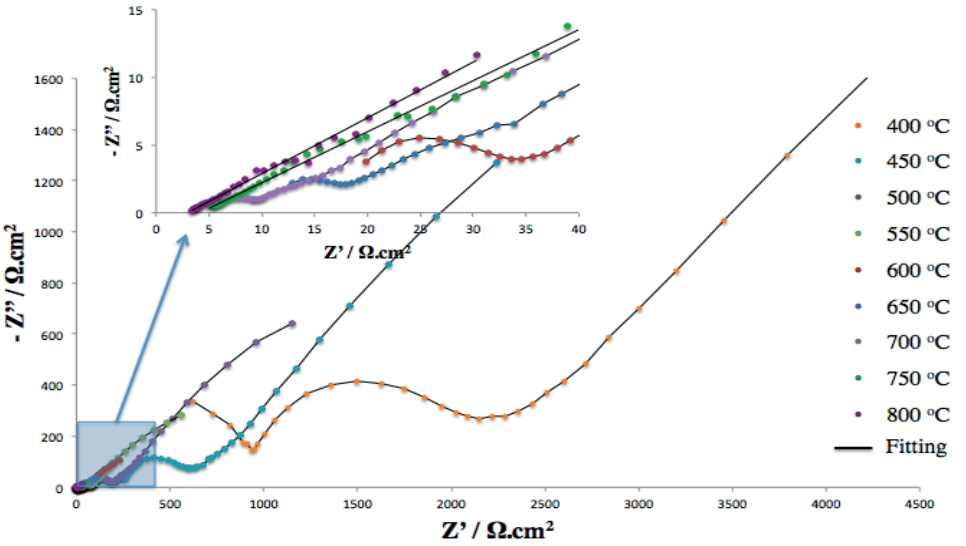

Supplementary Figure 11. Impedance spectra of LV05SM cathode measured in 15% O_2 and 85% N_2 at various temperatures with data fitting.

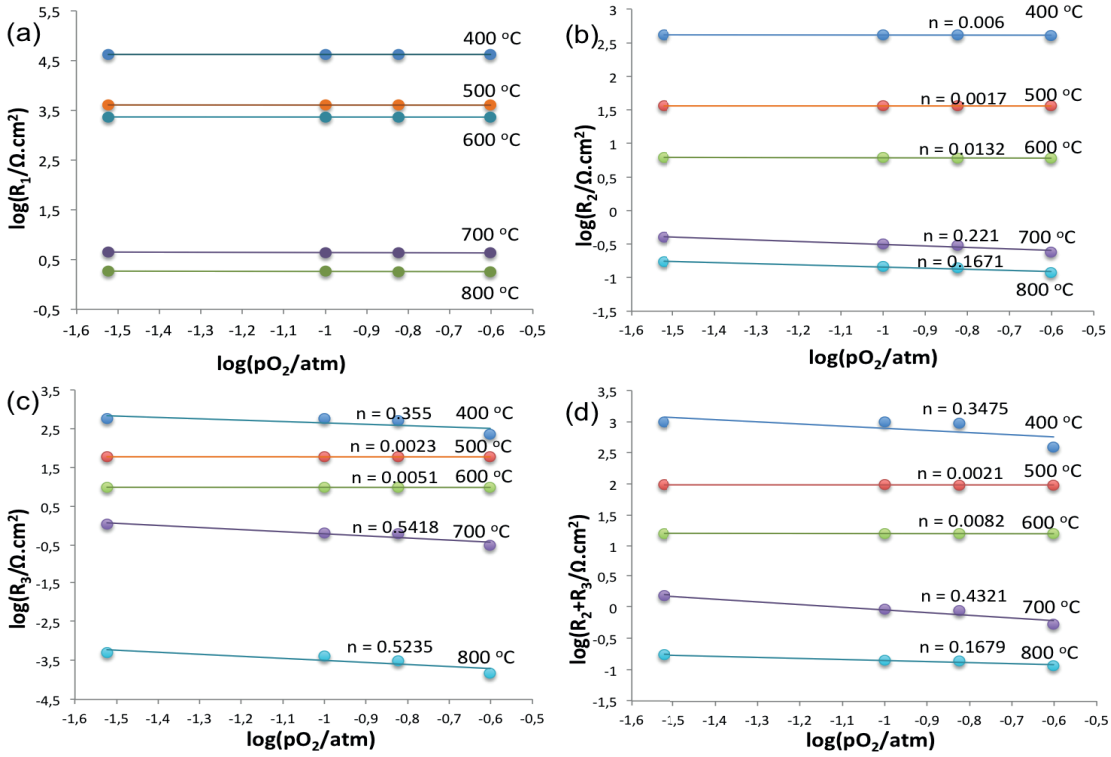

Supplementary Figure 12. Dependence of three resistances at high, medium, and low frequency on oxygen partial pressure for LV05SM/YSZ interface between 400 and 800 °C: a) R_1; b) R_2; c) R_3; d) R_2+ R_3.

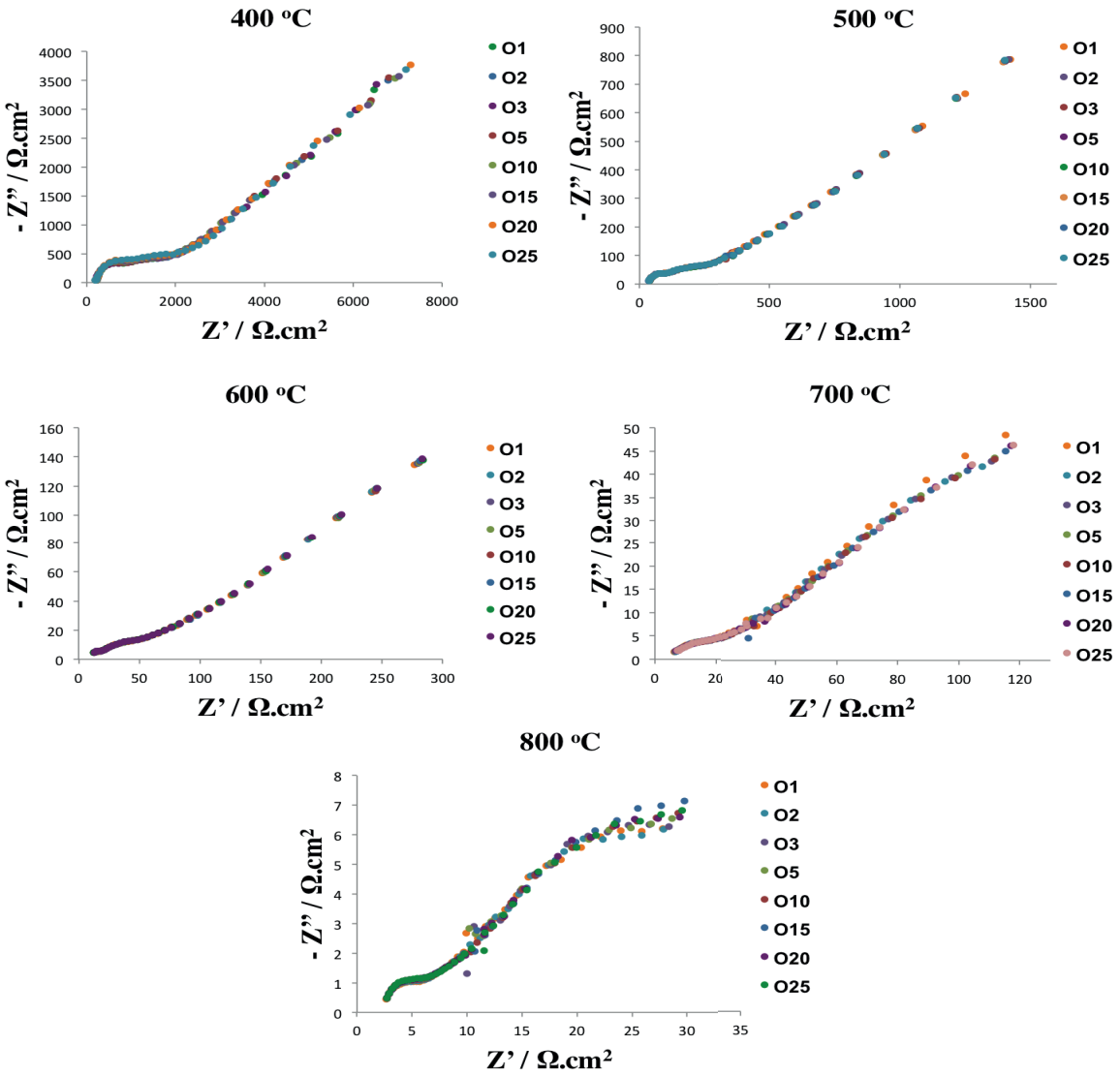

Supplementary Figure 13. Complex impedance plots for LV05SM/GDC/LV05SM symmetric cell at between 400 and 800 °C for different oxygen partial pressures.

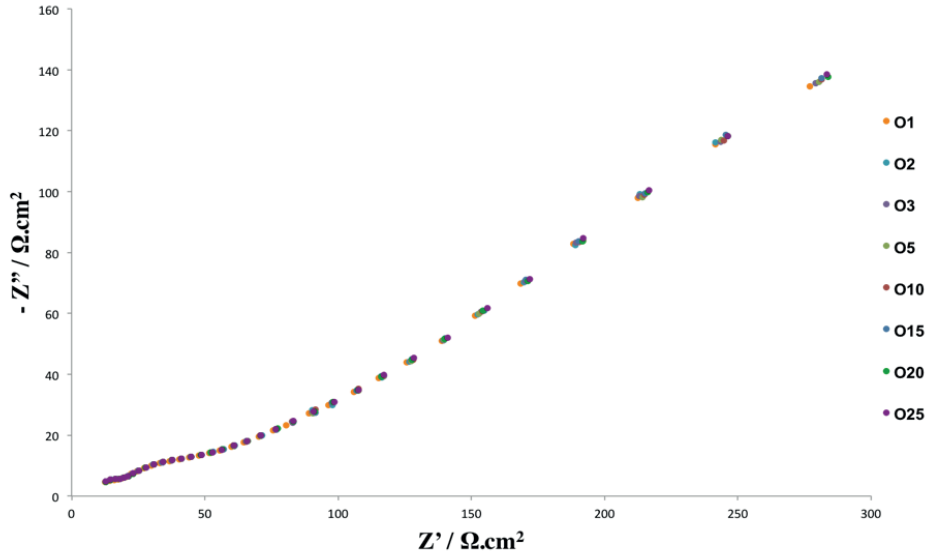

Supplementary Figure 14. Typical EIS of a symmetric LV05SM/GDC/LV05SM cell measured at 600 °C while fixing the oxygen partial pressure between 1% and 25%.

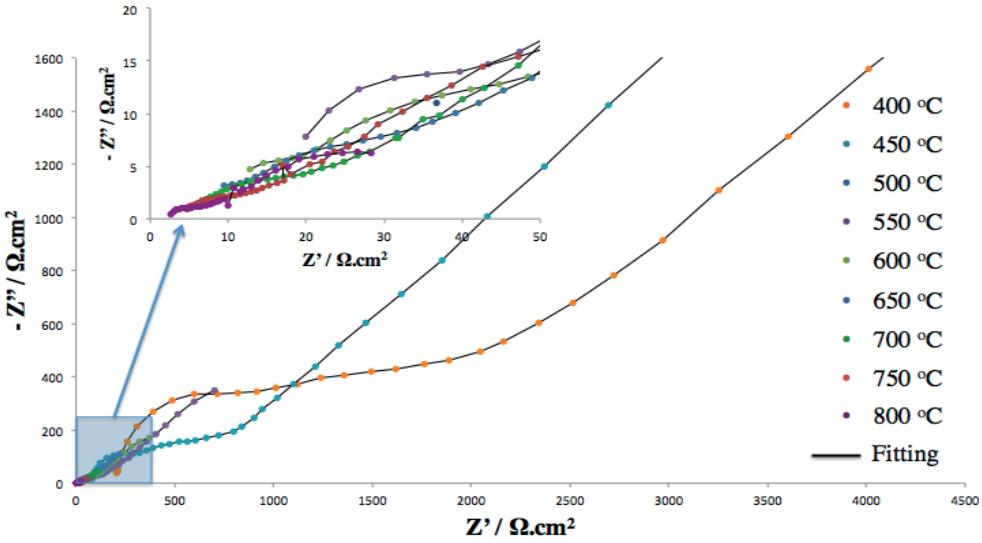

Supplementary Figure 15. Experimental and fit Nyquist plots for a symmetrical LV05SM/GDC/LV05SM cell measured at 3% O_2 and 97% N_2 between 400 and 800 °C.

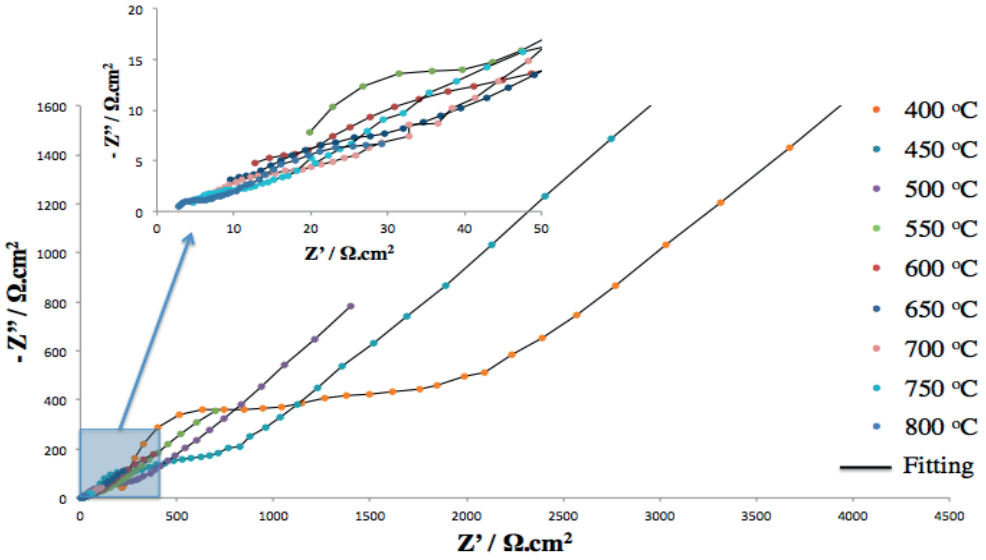

Supplementary Figure 16. Experimental and fit Nyquist plots for a symmetrical LV05SM/GDC/LV05SM cell measured at 10% O_2 and 90% N_2 between 400 and 800 °C.v

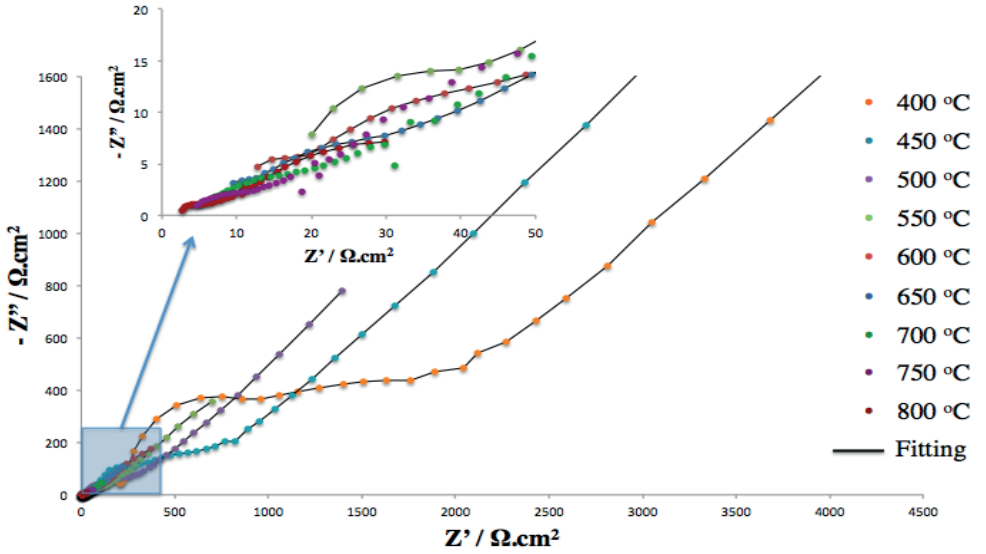

Supplementary Figure 17. Experimental and fit Nyquist plots for a symmetrical LV05SM/GDC/LV05SM cell measured at 15% O_2 and 85% N_2 between 400 and 800 °C.

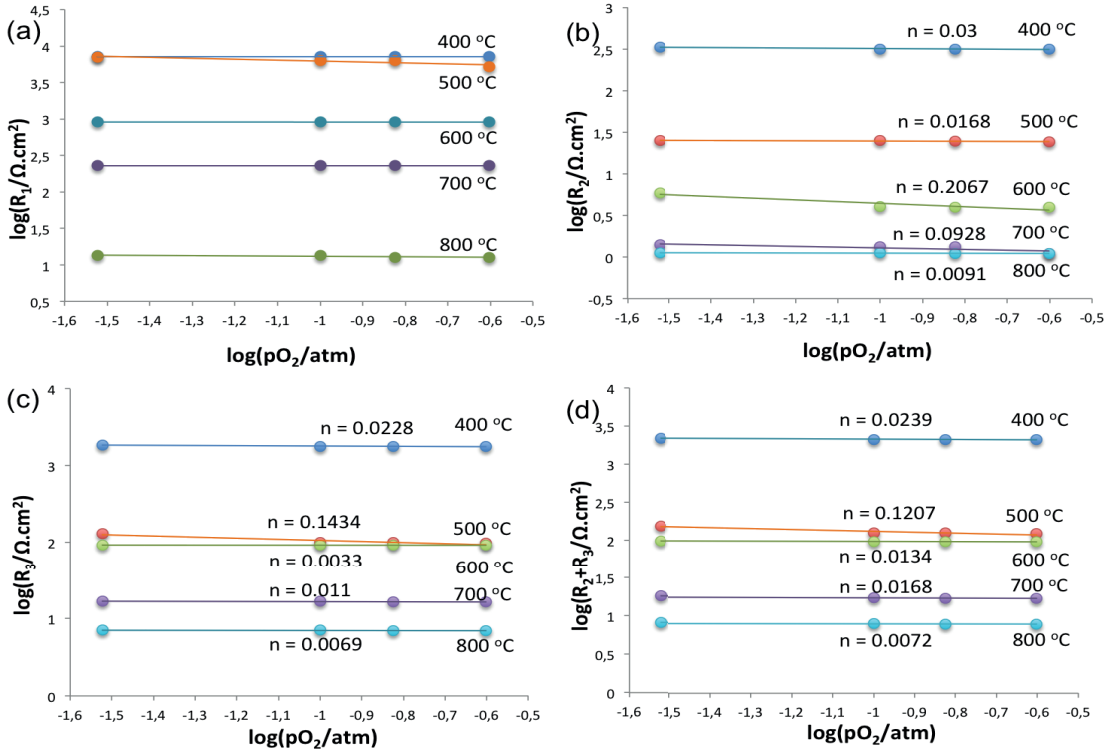

Supplementary Figure 18. Dependence of three resistances at high, medium, and low frequency on oxygen partial pressure for LV05SM/GDC interface between 400 and 800 °C: a) R_1; b) R_2; c) R_3; d) R_2+ R_3.